

Thermal Runaway During the Evolution of ONeMg Cores towards Accretion-Induced Collapse

Josiah Schwab^{1,2}, Eliot Quataert^{1,2}, Lars Bildsten^{3,4}

¹*Physics Department, University of California, Berkeley, CA 94720, USA*

²*Astronomy Department and Theoretical Astrophysics Center, University of California, Berkeley, CA 94720, USA*

³*Department of Physics, University of California, Santa Barbara, CA 93106*

⁴*Kavli Institute for Theoretical Physics, Santa Barbara, CA 93106*

Revision b07f982950e1c5e144321cabb4d3e80735c26383

ABSTRACT

We study the evolution of degenerate electron cores primarily composed of the carbon burning products ^{16}O , ^{20}Ne , and ^{24}Mg (hereafter ONeMg cores) that are undergoing compression. Electron capture reactions on $A = 20$ and $A = 24$ isotopes reduce the electron fraction and heat the core. We develop and use a new capability of the Modules for Experiments in Stellar Astrophysics (MESA) stellar evolution code that provides a highly accurate implementation of these key reactions. These new accurate rates and the ability of MESA to perform extremely small spatial zoning demonstrates a thermal runaway in the core triggered by the temperature and density sensitivity of the ^{20}Ne electron capture reactions. Both analytics and numerics show that this thermal runaway does not trigger core convection, but rather leads to a centrally concentrated ($r < \text{km}$) thermal runaway that will subsequently launch an oxygen deflagration wave from the center of the star. We use MESA to perform a parameter study that quantifies the influence of the ^{24}Mg mass fraction, the central temperature, the compression rate, and uncertainties in the electron capture reaction rates on the ONeMg core evolution. This allows us to establish a lower limit on the central density at which the oxygen deflagration wave initiates of $\rho_c \gtrsim 8.5 \times 10^9 \text{ g cm}^{-3}$. Based on previous work and order-of-magnitude calculations, we expect objects which ignite oxygen at or above these densities to collapse and form a neutron star. Calculations such as these are an important step in producing more realistic progenitor models for studies of the signature of accretion-induced collapse.

Key words: white dwarfs – stars:evolution

1 INTRODUCTION

In this paper, we study the evolution of degenerate electron cores primarily composed of the carbon burning products ^{16}O , ^{20}Ne , and ^{24}Mg which are undergoing compression. Such objects can arise in several contexts: the late stages of evolution for super asymptotic giant branch (SAGB) stars (e.g. Miyaji & Nomoto 1987; Ritossa et al. 1999; Takahashi et al. 2013; Jones et al. 2013), where the compression is caused by the deposition of material from exterior shell-burning; in a binary system with a massive ONeMg white dwarf (WD) (e.g. Nomoto & Kondo 1991), where the compression is caused by accretion from a non-degenerate companion; or as the remnant of a WD-WD merger, where the compression is caused by the cooling of the outer layers (e.g. Saio & Nomoto 1985).

As the core is compressed, the electron Fermi energy rises, eventually triggering exothermic electron capture reac-

tions. Typically, exothermic captures on ^{20}Ne release enough energy to cause thermonuclear ignition of ^{16}O and formation of a deflagration. The final fate of the core (either explosion or collapse) is determined by a competition between the energy release from the outgoing oxygen deflagration and the energy losses and decline in the electron fraction due to electron captures on the post-deflagration material, which has burned to nuclear statistical equilibrium (NSE). The evolution of these cores has been a subject of considerable previous study (e.g. Miyaji et al. 1980; Nomoto 1984; Isern et al. 1991; Canal et al. 1992; Gutierrez et al. 1996; Gutiérrez et al. 2005; Jones et al. 2014).

However, we revisit this topic (i) to test the effect of using the state-of-the-art Modules for Experiments in Stellar Astrophysics (MESA) stellar evolution code (Paxton et al. 2011, 2013, 2015), (ii) to demonstrate the effects of using the latest nuclear reaction rates (Martínez-Pinedo et al. 2014),

(iii) to perform a more detailed parameter study of the effects of a number of quantities, including the accretion rate \dot{M} , magnesium mass fraction X_{Mg} , and initial core temperature, T_c , and (iv) to provide analytic estimates of the evolution up-to and including the onset of the oxygen deflagration.

In the present paper, we follow the common treatment in the literature and parameterize the evolution of ONeMg WDs as they approach the Chandrasekhar mass via compression of the outer layers. In future work we will assess whether the revised evolutionary model of WD merger remnants proposed by Shen et al. (2012) and Schwab et al. (2012) modifies the likelihood of AIC in super-Chandrasekhar WD mergers. In § 2 we describe the treatment of weak reactions in the MESA code. In § 3 we provide analytic estimates relevant to the evolution of the core. In § 4 we discuss the inputs to our MESA calculations and in § 5 present the results of these numerical simulations. § 6 discusses the final fate of these cores. In § 7 we draw our conclusions and describe some important avenues for future work.

2 WEAK REACTIONS IN MESA

Weak reactions, specifically electron-capture and beta-decay, are central to the evolution of accreting degenerate ONeMg cores. The reduction in electron fraction (and corresponding reduction in pressure) due to electron captures accelerates the contraction of the cores and the entropy generation from these electron captures can directly ignite thermonuclear reactions.

This study makes use of MESA, a state-of-the-art open source code for stellar evolution calculations (Paxton et al. 2011, 2013). In particular we use the capability to calculate weak reaction rates directly from nuclear level and transition data, which is documented in the upcoming MESA Instrument Paper III (Paxton et al. 2015). This section summarizes the input data to this capability. The precise expressions which are evaluated as part of MESA’s on-the-fly weak reaction treatment are given in Appendix A.

We restrict ourselves to considering only a small set of $A = 24$ isotopes (^{24}Mg , ^{24}Na , ^{24}Ne) and $A = 20$ isotopes (^{20}Ne , ^{20}F , ^{20}O). Over the range of thermodynamic conditions encountered during the evolution of ONeMg cores, roughly $9 \lesssim \log_{10} \rho \lesssim 10$ and $8 \lesssim \log_{10} T \lesssim 9$ (in cgs units), Takahara et al. (1989) identified the transitions that dominate the rate of each reaction. We consider only this limited set of transitions; they are listed in Table 1. We have taken the comparative half-lives of these reactions from the up-to-date information compiled in Martínez-Pinedo et al. (2014).

In order to more easily visualize the data in Table 1, we present energy level diagrams for the $A = 24$ (Fig. 1) and $A = 20$ (Fig. 2) nuclei. These figures are modeled after those found in Takahara et al. (1989). The level structure of these nuclei is drawn from recent compilations of nuclear data (Tilley et al. 1998; Firestone 2007). We show all of the low-lying states that we consider, labeled with their J^π (spin^{parity}) values. The arrows indicate the limited set of transitions that we consider, which are only those which are “allowed” (Gamow-Teller: $J_i = J_j, J_j \pm 1, \pi_i \pi_j = 1$; excluding $J_i = J_j = 0$).

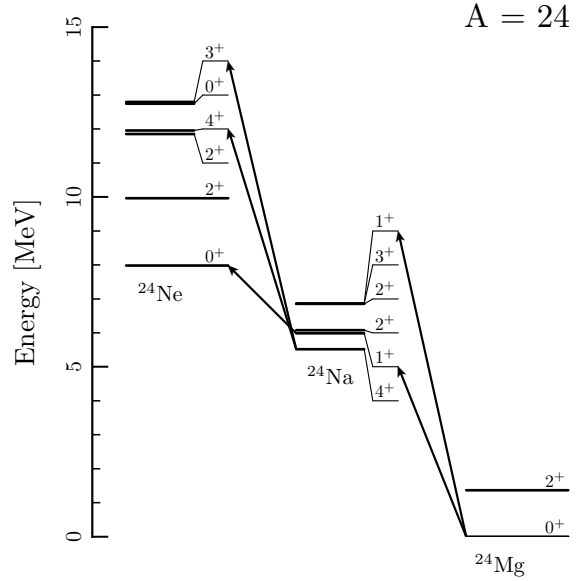


Figure 1. Energy level diagram for the $A = 24$ nuclei that we consider. The J^π values are sometimes given an arbitrary offset (indicated via thin lines) in order to enhance legibility. The transitions we consider are indicated with arrows.

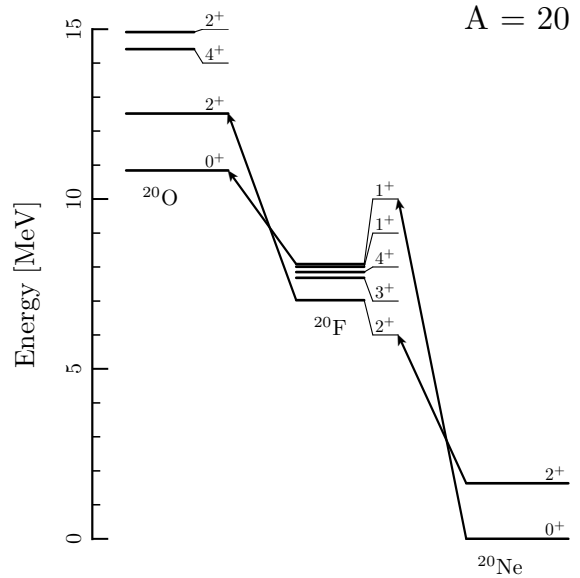


Figure 2. Energy level diagram for the $A = 20$ nuclei that we consider. The J^π values are sometimes given an arbitrary offset (indicated via thin lines) in order to enhance legibility. The transitions we consider are indicated with arrows.

3 ANALYTIC ESTIMATES

Miyaji et al. (1980) provide a thorough discussion of the different phases of the evolution of an ONeMg core undergoing compression. In order to gain some insight into the relevant physics, we first discuss a simple model of the evolution up until the onset of thermonuclear oxygen burning.

Initial	Final	Q_g	E_i	J_i^π	E_f	J_f^π	$\log_{10}(ft)$
^{24}Mg	^{24}Na	5.515	0.000	0^+	0.472	1^+	4.815
			0.000	0^+	1.347	1^+	3.838
^{24}Na	^{24}Ne	2.467	0.000	4^+	3.972	4^+	6.209
			0.000	4^+	4.866	3^+	4.423
			0.472	1^+	0.000	0^+	4.829
^{20}Ne	^{20}F	7.025	1.634	2^+	0.000	2^+	4.970
			0.000	0^+	1.057	1^+	4.380
			0.000	0^+	0.000	2^+	<i>9.801</i>
^{20}F	^{20}O	3.815	0.000	2^+	1.674	2^+	5.429
			1.057	1^+	0.000	0^+	4.211

Table 1. The transitions used in the rate calculations. They are written as electron capture transitions, but the same transitions were used for beta-decay (swapping initial and final states). Q_g is the energy difference between the ground states of the isotopes. E_i and E_f are respectively the excitation energies of the initial and final states, relative to the ground state. J_i^π and J_f^π are the spins and parities of the initial and final states. Allowed transitions do not have parity changes. (ft) is the comparative half-life in seconds, taken from Martínez-Pinedo et al. (2014) by dividing the constant 6144 s by their tabulated values of the transition matrix elements. The italicized (ft) value indicates an experimental upper limit; the effects of this transition will be discussed in § 5.3. All energies are in MeV. For level diagrams which illustrate the transitions, see Figs. 1 and 2.

In discussing the analytic estimates below, we reference some of the numerical results from our fiducial MESA model for comparison. This model is a cold ONeMg WD ($X_{\text{O}} = 0.5$, $X_{\text{Ne}} = 0.45$, $X_{\text{Mg}} = 0.05$) accreting at $\dot{M} = 10^{-6} M_{\odot} \text{yr}^{-1}$.

3.1 Overview of evolution

We have a dense, degenerate core near the Chandrasekhar mass with a spatially-uniform composition of the carbon-burning products ^{16}O , ^{20}Ne and ^{24}Mg , with mass fractions X_{O} , X_{Ne} , X_{Mg} , respectively. Fiducially, we choose $X_{\text{O}} = 0.5$, $X_{\text{Ne}} = 0.45$, $X_{\text{Mg}} = 0.05$. This is similar to the central abundances observed in recent calculations of the evolution of intermediate mass stars that develop these cores (see e.g., figure 10 of Takahashi et al. 2013). Other recent models of super-AGB evolution (Farmer et al. 2015) show typical central magnesium fractions $X_{\text{Mg}} \approx 0.03$ in the cases where the carbon deflagration wave reaches the center (R. Farmer, private communication).

The degenerate core is “accreting” at a rate \dot{M} ; such accretion might be set by carbon shell burning in an evolved star, accretion from a companion in a binary system, or cooling (and the concomitant reduction in pressure support) of the outer layers of a WD merger remnant. The key impact is that the core is being compressed on a timescale

$$t_{\text{compress}} = \left(\frac{d \ln \rho_c}{dt} \right)^{-1} = \left(\frac{d \ln \rho_c}{d \ln M} \right)^{-1} \frac{M}{\dot{M}}. \quad (1)$$

For an object supported by degeneracy pressure and in hydrostatic equilibrium, the central density rises rapidly as one approaches the Chandrasekhar mass. Therefore, the compression timescale is significantly shorter than the timescale for the growth of the core. For an ideal, zero-temperature

white dwarf, in the range $9 \lesssim \log_{10} \rho_c \lesssim 10$,

$$\frac{d \ln \rho_c}{d \ln M} \approx 28 \left(\frac{\rho_c}{10^9 \text{ g cm}^{-3}} \right)^{0.55}, \quad (2)$$

which we obtained by calculating a sequence of models and fitting a power-law to the results. This implies

$$t_{\text{compress}} \approx 5 \times 10^4 \text{ yr} \left(\frac{\rho_c}{10^9 \text{ g cm}^{-3}} \right)^{-0.55} \left(\frac{\dot{M}}{10^{-6} M_{\odot} \text{ yr}^{-1}} \right)^{-1}. \quad (3)$$

The dynamical time of the white dwarf is extremely short

$$t_{\text{dyn}} \approx \frac{1}{\sqrt{G\rho}} \approx 10^{-1} \text{ s} \left(\frac{\rho}{10^9 \text{ g cm}^{-3}} \right)^{-1/2} \quad (4)$$

and so hydrostatic equilibrium will always be preserved (until collapse ensues, which we do not study in detail in this paper).

The temperature of the core will be influenced by details of its previous evolution, such as the accretion history and by the abundances of isotopes which participate in Urca process cooling. However, if the compression timescale (and hence overall evolutionary timescale) is sufficiently slow, heating from compression and cooling from thermal neutrinos will reach a quasi-equilibrium (Paczynski 1971). Define the cooling time

$$t_{\text{cool}} = \frac{c_P T}{\epsilon_\nu}, \quad (5)$$

where c_P is the specific heat at constant pressure and ϵ_ν is the specific neutrino cooling rate. Then the relation $t_{\text{cool}} = t_{\text{compress}}$ implicitly defines a temperature for a given density and will characterize the thermal state of the core aside from periods when e-captures rapidly release energy. In Fig. 3, we show this relation as a blue, dashed line and demonstrate that our MESA models (the black solid line) described in § 4 and § 5 exhibit this relationship.

3.2 Effects of electron captures

As the core is compressed, the electron chemical potential increases. At zero temperature, the electron captures would occur when the Fermi energy reached the energy difference between the initial and final nuclear states. We refer to the density corresponding to this value of the chemical potential as the threshold density; the terms sub-threshold and super-threshold reference this density. At non-zero temperature, even when the chemical potential is below this threshold, there are some electrons in the high energy tail of the Fermi-Dirac distribution which are available to capture. As a result, the electron capture rate has an exponential dependence on the density and temperature in the sub-threshold case.

A simple form for the sub-threshold capture rate can be obtained by expanding equation (A15) in the limit that $\mu + Q \ll -kT$ (where μ is the chemical potential and $Q = Q_g + E_i - E_f$ is the energy difference between the parent and daughter nuclear state) and assuming that the rate is dominated by a single transition that begins in the ground state,

$$\lambda_{\text{ec}} \approx \frac{2 \ln 2}{(ft)} \left(\frac{kT}{m_e c^2} \right)^5 \left(\frac{Q}{kT} \right)^2 \exp \left(\frac{\mu + Q}{kT} \right). \quad (6)$$

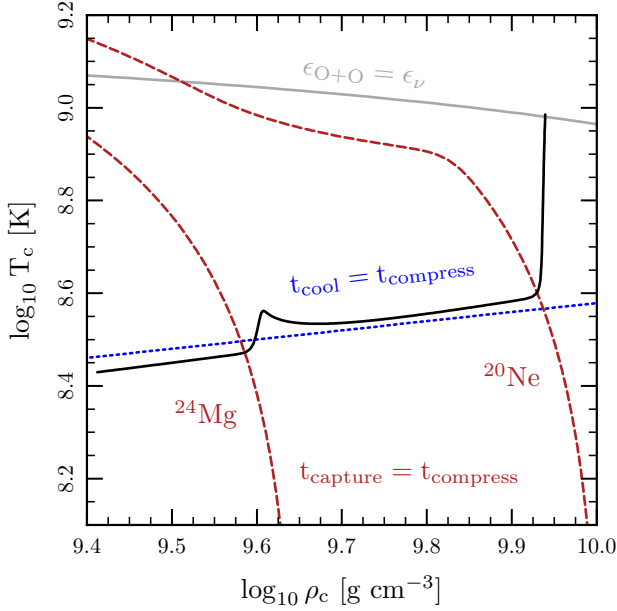


Figure 3. The black solid line shows the central density and temperature of the core as it is compressed with a surface accretion rate of $\dot{M} = 10^{-6} M_{\odot} \text{yr}^{-1}$ for approximately 20000 years of evolution. The red dashed lines indicate when the capture timescales for ^{24}Mg and ^{20}Ne become equal to the fiducial compression time of 10^4 yr. The blue dotted line shows where the neutrino cooling time and compression time are equal. This balance between compressional heating and neutrino cooling determines the thermal state of the contracting WD core (aside from brief periods when electron captures heat the core). The grey solid line shows where the energy generation from thermonuclear oxygen burning exceeds the thermal neutrino losses and we stop the calculation.

Define the capture timescale to be the inverse of the electron capture rate $t_{\text{capture}} = \lambda_{\text{ec}}^{-1}$. The onset of significant electron captures will occur when the capture time and the compression time become approximately equal. Setting $t_{\text{compress}} = t_{\text{capture}}$ gives an implicit relationship between ρ and T , which is a function of \dot{M} .

At zero temperature, the electron captures would occur at a density $\rho_{\text{ec},0}$ such that $\mu(\rho_{\text{ec},0}) + Q \approx 0$. Solving equation (6) for μ and rewriting the solution in terms of ρ , we find that $t_{\text{compress}} = t_{\text{capture}}$ when

$$\rho_{\text{ec}} \approx \rho_{\text{ec},0} \left[1 + \frac{3kT}{Q} \times \ln \left(2 \ln 2 \frac{t_{\text{compress}}}{(ft)} \left(\frac{kT}{m_e c^2} \right)^5 \left(\frac{Q}{kT} \right)^2 \right) \right], \quad (7)$$

where we have neglected the much weaker density dependence of t_{compress} itself.

Equation (7) will be valid up until a temperature at which the transition rate from an excited state, suppressed by $\exp(-E_i/kT)$, becomes the dominant contribution to the rate. As a rule of thumb, for the transitions we consider, this will happen when $T \approx E_i/(25k)$.

Fig. 4 shows numerical solutions for the location in density-temperature space at which $t_{\text{capture}} = 10^4$ yr (which is approximately the compression timescale associated with an $\dot{M} = 10^{-6} M_{\odot} \text{yr}^{-1}$) for ^{24}Mg , ^{24}Na , ^{20}Ne , and ^{20}F .

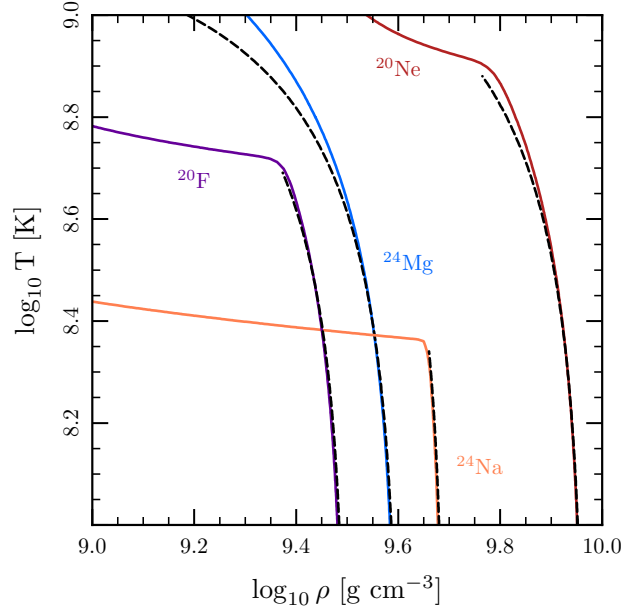


Figure 4. The solid lines show where the electron capture timescale is equal to 10^4 yr (which is approximately the compression timescale of the WD core for $\dot{M} = 10^{-6} M_{\odot} \text{yr}^{-1}$). At ρ and T greater than those delineated by the solid lines, the capture time is less than the compression time. Each line is labeled by the name of the isotope undergoing electron capture. The black dashed lines show the analytic approximation given in equation (7). For ease of comparison with the analytic results, the Coulomb corrections discussed in Appendix B are not present in these calculations.

The approximations for the critical density based on equation (7) are overlaid as dashed black lines and are in excellent agreement. The line for ^{20}F is always at lower density than that of ^{20}Ne , meaning once the first capture in the $^{20}\text{Ne} \rightarrow ^{20}\text{F} \rightarrow ^{20}\text{O}$ chain occurs, the second will immediately follow. This is not true for ^{24}Na relative to its parent ^{24}Mg , meaning the captures in the $^{24}\text{Mg} \rightarrow ^{24}\text{Na} \rightarrow ^{24}\text{Ne}$ chain will happen at separate densities when $\log_{10} T \lesssim 8.4$.

The electron captures also influence the temperature evolution of the core. When a capture occurs, the chemical potential of the captured electron, minus the change in nuclear rest mass and the energy in the emitted neutrinos, is thermalized, heating the plasma.¹ This heating is substantial, because the first capture is often into an excited state (meaning the chemical potential is higher when the rate of this transition becomes significant) and the second is typically super-threshold. Does this heating drive convection? If so, this convection will efficiently transport the entropy out of the core while mixing in fresh fuel for electron captures.

The electron captures generate entropy, creating a negative radial entropy gradient in the core. The captures also reduce the electron fraction in the core, creating a positive radial gradient in Y_e . The entropy gradient is destabilizing, but the Y_e gradient is stabilizing. Simulations which invoked the Schwarzschild criterion for convection (e.g. Miyaji et al.

¹ A more precise definition of the heating rate is given in Appendix A, specifically equations (A29) and (A30).

1980), which does not consider composition gradients, found that the captures do trigger convection. Simulations which invoke the Ledoux criterion, which does consider composition gradients, found that the captures do not trigger convection (e.g. Miyaji & Nomoto 1987). Hence the different choices lead to qualitatively different evolution.

The following calculation demonstrates why the electron captures are unable to trigger convection when accounting for stabilizing composition gradients. The Ledoux criterion for convective instability is

$$\nabla_{\text{ad}} - \nabla_T + B < 0 \quad (8)$$

where

$$B = -\frac{1}{\chi_T} \left(\frac{\partial \ln P}{\partial \ln Y_e} \right)_{\rho, T} \frac{d \ln Y_e}{d \ln P}. \quad (9)$$

The captures occur over a narrow range in Fermi energy, and hence density. Therefore the gradients in T and Y_e across the region where the captures occur will be large. This allows us to drop the ∇_{ad} term. Replacing the gradients with finite differences, we then check the inequality

$$\Delta(\ln T) > -\frac{1}{\chi_T} \left(\frac{\partial \ln P}{\partial \ln Y_e} \right)_{\rho, T} \Delta(\ln Y_e). \quad (10)$$

For a cold plasma with degenerate electrons and ideal ions, $(\partial \ln P / \partial \ln Y_e)_{\rho, T} \approx 4/3$ and $\chi_T \approx 4kT / (\bar{Z}E_F)$. If a mass fraction ΔX_c has undergone electron captures, the associated change in temperature is

$$\Delta T \approx \frac{\bar{A}}{A_c} \left(\frac{E_c}{c_P} \right) \Delta X_c, \quad (11)$$

where A_c is the nuclear mass number of the species that is capturing and E_c is the average energy deposited by a capture. At the typical densities and temperatures in our calculation, the ions are a Coulomb liquid and so $c_P \approx 3k$. The change in Y_e due to the captures is

$$\Delta Y_e \approx \frac{\Delta Z}{A_c} \Delta X_c. \quad (12)$$

Both the $A = 24$ and $A = 20$ chains that we consider are two electron captures long, so we set $\Delta Z = -2$.

Substituting these estimates into equation (10) and simplifying, the condition for convective instability becomes

$$\frac{E_c}{E_F} > 2. \quad (13)$$

This inequality demonstrates that in order to trigger convective instability, the two captured electrons—which each have a characteristic energy of E_F —would have to deposit nearly all their energy as thermal energy. This is unrealistic, since substantial amounts of energy go into the rest mass of the daughter nucleus and to neutrinos. From our calculation of the heating rates, it is clear this inequality is far from being violated: the $A = 24$ captures occur at $E_F \approx 6.5$ MeV and release $E_c \approx 0.5$ MeV; the $A = 20$ captures occur at $E_F \approx 8.5$ MeV and release $E_c \approx 3$ MeV. Electron captures do not directly trigger convection.

A region which is Schwarzschild-unstable but Ledoux-stable is semiconvective. The semiconvective diffusion coefficient used in MESA (Paxton et al. 2013, following Langer et al. 1983) is

$$D_{\text{sc}} = \alpha_{\text{sc}} \left(\frac{K}{6c_P \rho} \right) \left(\frac{\nabla_T - \nabla_{\text{ad}}}{B + \nabla_{\text{ad}} - \nabla_T} \right), \quad (14)$$

where K is the radiative conductivity. The values of α_{sc} , the semiconvective efficiency adopted in the literature span the range $10^{-3} \lesssim \alpha_{\text{sc}} \lesssim 1$ (Paxton et al. 2013, citing Langer 1991; Yoon et al. 2006).

Regions where the electron captures have not yet occurred and regions where they have completed do not have a Y_e gradient. Therefore the width of the semiconvective zone H_{sc} will be roughly the length over which the density changes by an amount that shifts E_F by kT . We expect

$$H_{\text{sc}} \sim 4 \left(\frac{kT}{E_F} \right) H_P \quad (15)$$

where H_P is the pressure scale height. Defining $f = H_{\text{sc}}/H_P$, we find $f \approx 0.03$ in our MESA models, consistent with the above estimate. We define the timescale for semiconvection to modify the composition and thermal structure in our models as

$$t_{\text{sc}} = \frac{H_{\text{sc}}^2}{D_{\text{sc}}} \sim 3 \times 10^4 \text{ yr} \left(\frac{1}{\alpha_{\text{sc}}} \right) \left(\frac{f}{0.03} \right)^2. \quad (16)$$

For $\alpha_{\text{sc}} \lesssim 1$, t_{sc} in equation (16) is equal to or longer than time that elapses between ^{24}Mg captures and oxygen ignitions in our fiducial model. Moreover, t_{sc} is an upper limit: because of the thinness of the region with a Y_e -gradient, an individual parcel spends less time in a semiconvective region. Therefore, we do not consider semiconvection in our models.

For realistic ^{24}Mg fractions, e-captures on ^{24}Mg do not release enough energy to initiate thermonuclear fusion. As a result, the core continues to compress and we eventually reach the density where the captures begin on the $A = 20$ nuclei. Once the capture on ^{20}Ne occurs, the capture on ^{20}F occurs immediately. Like the $A = 24$ captures, the bulk of the energy deposition comes from this super-threshold capture, but in this case the energy per capture is substantially greater, $E_c \approx 3$ MeV. The characteristic temperature for oxygen ignition is approximately 10^9 K and so from equation (11), we estimate that oxygen will ignite after an amount $\Delta X_{\text{Ne}} \approx 0.1$ has undergone capture. We halt our main MESA calculations when the energy generation rate from oxygen burning exceeds the cooling from neutrinos, implying that a nuclear runaway is assured.

We have focused primarily on the evolution of the center of the core, but the density of the rest of the core increases during compression. Electron captures on the $A = 24$ elements have been occurring off-center as parcels of the star reach conditions favorable for these captures. This is illustrated in Fig. 5, where one can see the depletion of ^{24}Mg in the inner $0.3M_{\odot}$ of the star.

3.3 Thermal runaway from ^{20}Ne Captures and Oxygen Deflagration Initiation

In Fig. 6 we show the evolution of the center of our MESA models as the $A = 20$ captures begin.² The profiles are labeled by the central heating time of the model, $t_{\text{heat},c} = c_p T / \epsilon_{\text{nuc}}$. At these temperatures, the energy generation rate

² The MESA run shown in this plot used a finer central spatial and temporal resolution than our fiducial case in order to better resolve the onset of these steep central gradients.

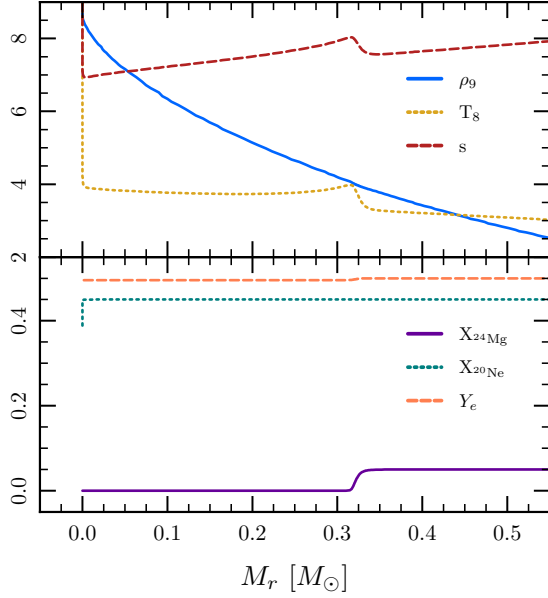


Figure 5. The structure of the model from Fig. 3 at the end of the MESA calculation (when the energy generation rate from oxygen burning exceeded the neutrino cooling). The top panel shows the density (ρ_9 , ρ in units of 10^9 g cm^{-3}), the temperature (T_8 , T in units of 10^8 K), and the entropy per baryon s (in units of k), as a function of enclosed mass. The bottom panel shows the mass fractions of ^{24}Mg and ^{20}Ne as well as the electron fraction Y_e . The small region in which there is a Y_e gradient due to the $A = 24$ captures has been moving outward in a Lagrangian sense. By the time the center reaches the density for ^{20}Ne captures, the inner $0.3M_\odot$ has already been depleted of ^{24}Mg due to e-captures. The subsequent evolution is discussed in § 6.

is dominated by the $A = 20$ captures, which are undergoing a thermal runaway in the thermally conducting core. From equation (11), the change in Y_e associated with increasing the temperature from its value before the $A = 20$ captures, $T \approx 4 \times 10^8 \text{ K}$, to the temperature for oxygen ignition, $T \approx 10^9 \text{ K}$, is $\Delta Y_e \approx 0.006$, in good agreement with the change observed in the lower panel of Fig. 6. Changes in T and Y_e will no longer be so tightly coupled once energy release from oxygen fusion exceeds that from electron captures, pushing the core towards convective instability. However, in order to reach convective instability, equation (10) requires

$$\Delta T > \frac{\bar{A}E_F}{3k} \Delta Y_e \approx 3.5 \times 10^9 \text{ K} \left(\frac{\Delta Y_e}{0.006} \right), \quad (17)$$

a temperature so large that the central heating timescale from oxygen fusion would be $t_{\text{heat},c} \approx 10^{-5} \text{ s}$. We show here that a thermal runaway is triggered long before such a condition is reached.

The $A = 20$ electron captures occur in an environment where the electron Fermi energy is below the energy threshold. In this sub-threshold case, those electrons that capture are on the thermal tail of the distribution, making the rate very sensitive to both density and temperature.³ We now

³ Because the bulk of the heating comes from the super-threshold

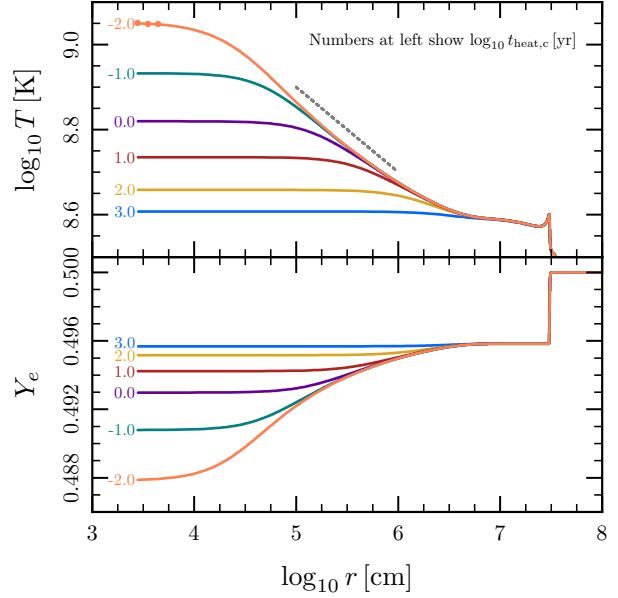


Figure 6. The temperature (T) and electron fraction (Y_e) profiles in the MESA model shown in Fig. 5, as it is approaching the onset of O fusion. At these temperatures, the energy release is dominated by the $A = 20$ captures, so T and Y_e are closely tied. The lines are labeled by the heating timescale at the center of the model. The dotted grey line in the top panel shows the slope of the temperature profile expected for a thermal runaway with diffusion. The mass resolution in this calculation is significantly higher than that in other figures in order to resolve the small region (regulated by thermal diffusion) within which thermal runaway sets in. The dots on the orange (hottest) temperature curve indicate the locations of the innermost three MESA zones; the mass in the central zone is roughly $4 \times 10^{-13} M_\odot$.

show that this naturally leads to a local thermal runaway in the core whose size is limited by thermal conduction. This runaway provides the “hot-spot” needed to initiate the oxygen deflagration from the center of the star.

The strong density sensitivity of the $A = 20$ captures implies that the runaway will begin at the exact center of the isothermal core. However, the pressure declines away from the core, leading to a temperature gradient on the scale over which the electron capture rate (and hence the heating rate) varies by order unity. In this sub-threshold case, $d \ln \lambda / d \ln P = E_F / (4kT)$, so the change in pressure needed to have the rate be less at the outer edge than the center is

$$\Delta P \approx 4P_c \left(\frac{kT}{E_F} \right) \approx \left(\frac{\rho_c Y_e}{m_p} \right) kT_c. \quad (18)$$

Hydrostatic equilibrium provides such a pressure change over a length scale

$$l_T = \left(\frac{3\Delta P}{2\pi G \rho_c^2} \right)^{1/2} \approx 4 \times 10^6 \text{ cm}, \quad (19)$$

where we have used $T_c \approx 4 \times 10^8 \text{ K}$ and $\rho_c \approx 9 \times 10^9 \text{ g cm}^{-3}$,

electron capture on ^{20}F that immediately follows the ^{20}Ne capture, the capture rate on ^{20}Ne is a good proxy for the temperature and density dependence of the heating rate.

corresponding to the onset of $A = 20$ captures in our fiducial model. This estimate is consistent with the length scale observed at the onset of the runaway in Fig. 6.

The subsequent evolution of the runaway is driven by the temperature sensitivity of the sub-threshold electron capture rate. This rate is well-approximated by equation (6), yielding a logarithmic derivative of the rate with respect to temperature of

$$\frac{d \ln \lambda}{d \ln T} = 3 - \frac{\mu + Q}{kT}. \quad (20)$$

Physically, the second term is the how far the transition is below its threshold energy (in units of kT). As in the $A = 24$ case, electron captures become important when $\lambda_{\text{ec}}^{-1} \approx t_{\text{compress}}$; from equation (6) this occurs at $(\mu + Q)/(kT) \approx -14$. The thermal runaway is sufficiently rapid that $\mu + Q$ remains approximately fixed. This implies that the captures will be extremely temperature sensitive, scaling as $\lambda \propto T^n$, where

$$n \equiv \frac{d \ln \lambda}{d \ln T} \approx 3 + 14 \left(\frac{T}{4 \times 10^8 \text{ K}} \right)^{-1}. \quad (21)$$

In the following estimates, we will take $n \approx 12$, and since $n \gg 1$, we will treat $n \approx n \pm 1$.

Hence, as captures begin, their density dependence leads to a temperature gradient on the length scale given by equation (19). Because convection is not initiated, the heating remains local, and this temperature gradient will grow with time in a thermal runaway. Once it is sufficient to cause an order unity variation of the capture rate across a given length r , the gradient will become non-linear. The hotter part will begin to evolve more rapidly and the evolution of the cooler part will freeze-out. This will occur when $dT/dr \approx (T/n)/r$ and so on its own, thermal runaway leads to a characteristic profile where $d \ln T/d \ln r \approx 1/n$. However, thermal conduction limits the volume that can runaway to a fixed temperature, keeping regions where $t_{\text{th}} \lesssim t_{\text{heat}}$ approximately isothermal. The thermal diffusivity from electron conduction is $D_{\text{th}} \approx 30 \text{ cm}^2 \text{ s}^{-1} (T/10^9 \text{ K})$, meaning that the timescale for conduction to modify the thermal structure over a lengthscale r is

$$t_{\text{th}} = \frac{r^2}{D_{\text{th}}} \approx 10^3 \text{ yr} \left(\frac{r}{10^6 \text{ cm}} \right)^2 \left(\frac{T}{10^9 \text{ K}} \right)^{-1}. \quad (22)$$

Therefore, the size of the isothermal region at the center of the model scales like $r \propto T_c^{1-n/2}$. Thus, as the runaway progresses, it will create a temperature profile with $d \ln T/d \ln r \approx -1/5$. The dotted grey line in the top panel of Fig. 6 shows this slope, which agrees well with the temperature evolution in the MESA calculations. The semiconvective instability grows on the thermal diffusion time. During the thermal runaway, by definition, $t_{\text{heat}} \lesssim t_{\text{th}}$. Hence, the evolution of the core during this phase will be sufficiently fast that semiconvection will not modify the temperature or composition.

This thermal runaway leads to a small volume at the core reaching very high temperatures, eventually to values large enough for heating from oxygen fusion to play a role. This occurs when $T \approx 1.1 \times 10^9 \text{ K}$, where the heating time is $t_{\text{heat}} \approx 10^{-2} \text{ yr}$. From equation (22), the hottest (isothermal, so $t_{\text{th}} \approx t_{\text{heat}}$) part of the core will have a size $r \approx 3 \times 10^3 \text{ cm}$, which encompasses about 3×10^{-13} of the total mass.

The finest central zoning that we were able to achieve in our MESA calculations (as shown in Fig. 6) was a mass resolution of approximately $4 \times 10^{-13} M_{\odot}$. Therefore, just as oxygen burning begins to dominate the energy release, the small size of this region prevents us from continuing to follow its evolution in our full star MESA simulations.

The conditions created in the core of the star as energy generation by oxygen fusion begins to dominate over $A = 20$ captures lead naturally to the development of an oxygen deflagration wave. In particular, we have shown that oxygen fusion begins in a region at the core of the star whose size is determined by $t_{\text{th}} \lesssim t_{\text{heat}}$. With t_{heat} identified as the heating time associated with oxygen fusion, this is precisely the condition for the onset of an oxygen deflagration wave; Timmes & Woosley (1992) defined the deflagration ‘‘trigger mass’’ to be the mass contained within the region satisfying this constraint. Therefore, we are confident that the hot central region present at the end of our MESA calculations, being unstable to thermal runaway, will continue to grow in temperature and shrink in size, eventually reaching the laminar deflagration solutions of Timmes & Woosley (1992).⁴ The outgoing deflagration wave will sweep across this thermally unstable core in less than one second.

It is important to stress that the onset of the oxygen deflagration in the AIC context is substantially different than the ‘‘simmering phase’’ in single degenerate Type Ia supernovae progenitors. There, after pycnonuclear carbon ignition occurs, the entropy release from carbon burning drives the formation of a central convection zone. The growth and heating of this convective zone lead to a significant decrease in the central density between the time of carbon ignition and the development of a deflagration.

In our models, by contrast, no central mixing occurs because of the stabilizing effect of the composition gradient associated with $A = 20$ captures. Therefore the central density at which oxygen ignition occurs, and at which we halt our MESA calculations, is a good estimate of the central density at which the oxygen deflagration develops. We discuss the propagation of this deflagration and its influence on the final outcome in § 6.

4 DETAILS OF MESA CALCULATIONS

All of the calculations performed in this paper are based on revision 6596 (released 2014-06-07), with some modifications to support our weak rate calculations. The incorporation of these changes into the mainline MESA code will be discussed in the upcoming MESA Instrument Paper III (Paxton et al. 2015). As required by the MESA manifesto, the inlists and source code modifications necessary to reproduce our calculations will be posted on <http://mesastar.org>.

4.1 Generation of Initial Models

In order to perform the parameter study discussed § 5, it is necessary to have a set of models of ONeMg cores with

⁴ At the density in our MESA calculations, the laminar deflagration width is $\delta \approx 3 \times 10^{-5} \text{ cm}$, far below our ability to resolve in our full star simulations.

a range of different temperatures and compositions to use as initial conditions. We generate an idealized set of models via the following *ad hoc* steps. During each step, all nuclear reactions are turned off, ensuring that the model will continually contract until halted by degeneracy pressure.

We begin with a $1.325M_{\odot}$ pre-main sequence model of normal (roughly solar) composition. We evolve this model until it reaches a central density of $\log_{10} \rho = 3$ (cgs). We then relax the (homogeneous) composition to the desired ^{16}O , ^{20}Ne , and ^{24}Mg mass fractions and allow the model to evolve until the central density reaches $\log_{10} \rho = 7$. Then we set the model to accrete at a constant \dot{M} and evolve until the central density reaches $\log_{10} \rho = 9.4$, which is still below the threshold for the onset of the electron capture reactions of interest. In order to achieve different core temperatures, we vary \dot{M} ; models with higher (lower) accretion rates have less (more) time for neutrino cooling to carry away energy and are correspondingly hotter (colder). By this means, we arrive a set of models with varied compositions and central temperatures to use as initial models.

4.2 Important MESA Options

While our full inlists will be made publicly available, we highlight some of the most important MESA options used in the calculations. This section assumes the reader is familiar with specific MESA options. Please consult the instrument papers (Paxton et al. 2011, 2013) and the MESA website⁵ for a full explanation of the meaning of these options.

Since MESA is an implicit code, it is important that we choose timesteps that will resolve the processes of interest. The evolution of the ONeMg cores is driven by the increase in central density (and hence Fermi energy) caused by the ongoing compression. Therefore, our default runs include a timestep criterion based specifically on changes in central density

```
delta_lgRho_cntr_hard_limit = 3e-3
delta_lgRho_cntr_limit = 1e-3
```

in addition to the primary spatial and temporal convergence settings of

```
varcontrol_target = 1e-3
mesh_delta_coeff = 1.0 .
```

Evidence demonstrating that this set of MESA options yields a converged result is shown in Appendix C.

These calculations use a nuclear network based on the `co_burn.net` network included with MESA with the addition of the isotopes ^{20}O , ^{20}F , ^{24}Ne , and ^{24}Na and the weak reactions linking the $A = 20$ isotopes to ^{20}Ne and the $A = 24$ isotopes to ^{24}Mg . The special treatment of these weak reactions (as discussed in Appendix A) is activated with the options

```
use_special_weak_rates = .true.
ion_coulomb_corrections = 'PCR2009'
electron_coulomb_corrections = 'Itoh2002'
```

where the last two lines select the Coulomb corrections discussed in Appendix B.

⁵ <http://mesa.sourceforge.net>

5 PARAMETER STUDIES

In this section, we use a suite of MESA calculations to study how a variety of parameters affect the evolution of these cores. The key question we will answer is whether reasonable variation in these parameters will affect the final outcome.

The first parameter (§ 5.1), the initial ^{24}Mg mass fraction (X_{Mg}), is an intrinsic property of the ONeMg core, set during the process that produced the core. Variation in this value may reflect variation in the formation process (e.g., the initial mass of the star that produced it) as well as limits of our knowledge (e.g., uncertainties in quantities such as the $^{12}\text{C}(\alpha, \gamma)^{16}\text{O}$ reaction rate). The second parameter (§ 5.2), the accretion rate \dot{M} , is set by the current state of the system (e.g., the properties of a binary companion, the details of shell-burning). The third parameter (§ 5.3), the strength of the second forbidden transition between the ground states of ^{20}Ne and ^{20}F , reflects a limit in our current knowledge.

5.1 Effect of a ^{24}Mg mass fraction

Gutiérrez et al. (2005) performed a parameter study of the effects of the ^{24}Mg mass fraction. We follow their approach of varying the central ^{24}Mg fraction, while holding the $^{16}\text{O}/^{20}\text{Ne}$ ratio fixed.⁶ We explore a wide range of ^{24}Mg mass fractions, from 0.01 up to 0.20. This latter value is well above the expected ^{24}Mg fraction given current reaction rates. Our results are shown in Fig. 7.

The temperature increase due to the $A = 24$ electron captures scales roughly linearly with X_{Mg} , as expected from equation (11). For $X_{\text{Mg}} \lesssim 0.07$, neutrino cooling erases the effect of the heating and the trajectories converge back towards the $t_{\text{cool}} = t_{\text{compress}}$ relation described in § 3. Correspondingly, the density at which the captures on ^{20}Ne occur—and thus the density at which oxygen ignites—is independent of X_{Mg} . For $X_{\text{Mg}} \gtrsim 0.07$, an increase in X_{Mg} leads to the onset of ^{20}Ne captures (and oxygen ignition) at a higher density. At even higher values (not shown), the heating from the $A = 24$ captures is sufficient to directly ignite oxygen burning as noted by Miyaji & Nomoto (1987) and Gutiérrez et al. (2005).

In the limited set of models presented in Gutiérrez et al. (2005) this bifurcation in the core evolution around $X_{\text{Mg}} \approx 0.07$ is not evident. However, it has a clear physical explanation. In Appendix D we discuss a simple model of a zero-temperature white dwarf with a low- Y_e core that explains these results; here, we demonstrate the consistency of these calculations with our MESA models, eliding the details.

Fig. 8 shows the compression time in two models, one on each side of this threshold value of X_{Mg} . The core evolution for both models follows the dashed black line defined by equation (3) up until the onset of the $A = 24$ electron captures at $\log_{10} \rho_c \approx 9.6$. Above this density, the $X_{\text{Mg}} = 0.05$ model (blue line) follows the dotted line, which is the track expected for the fiducial value of \dot{M} and the

⁶ In accordance with our fiducial model, we set this ratio be at 10/9. The choice of this ratio does slightly influence the density at which captures occur through the dependence of the Coulomb corrections on Z . However, as a small shift on top of a small shift, we do not explore variations in this ratio.

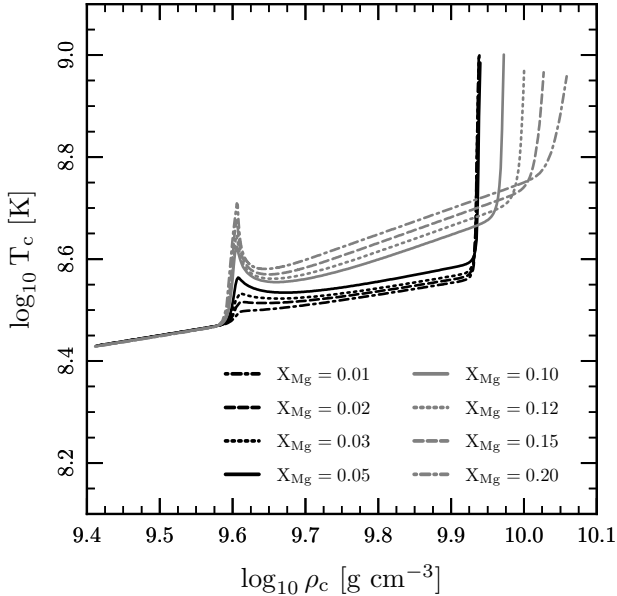


Figure 7. The evolution of the central density and temperature for different magnesium mass fractions. At lower X_{Mg} values, the density at which oxygen ignition occurs (the end of the track) is independent of X_{Mg} ; at higher X_{Mg} values, the density at which oxygen ignition occurs increases with increasing X_{Mg} . The text and Figs. 8 and 9 explain the origin of this trend.

value of $d \ln M / d \ln \rho_c$ in equation (1) calculated from a zero-temperature white dwarf model in which Y_e decreases for $\log_{10} \rho > 9.6$. See Fig. D1 and surrounding discussion for the details of this zero-temperature model.

In the $X_{\text{Mg}} = 0.15$ model (yellow line in Fig. 8), once the ^{24}Mg captures occur at $\log_{10} \rho_c \approx 9.6$, the compression timescale begins to fall dramatically. By the time ^{20}Ne capture densities are reached ($\log_{10} \rho \approx 10$), the compression timescale is orders of magnitude smaller than in the lower X_{Mg} models, though it remains significantly longer than the dynamical time. Recall that significant electron captures only occur when the capture time satisfies the relation $t_{\text{compress}} = t_{\text{capture}}$; this means that for shorter compression timescales, the core must reach higher densities, and hence higher capture rates, before the effects of the captures become apparent. As X_{Mg} increases, models experience a larger drop in Y_e , and compress more quickly. This explains the trend of increasing oxygen ignition density with increasing X_{Mg} seen in Fig. 7.

To physically understand the different evolution of the $X_{\text{Mg}} \gtrsim 0.07$ models, we consider an idealized model of the effect of Mg captures on the structure and stability of the ONeMg core. We assume that the $A = 24$ electron captures occur instantaneously above a density of $\rho_n = 9.6$. Using the approach described in Appendix D, we can then determine the central density of the zero temperature model with the maximum mass. The result of this calculation is shown as the dashed line in Fig. 9. Any model with $X_{\text{Mg}} \gtrsim 0.07$ will cross the stability line before the onset of ^{20}Ne captures. Moreover, for a larger change in Y_e (associated with a larger X_{Mg} in the current example), the onset of instability occurs

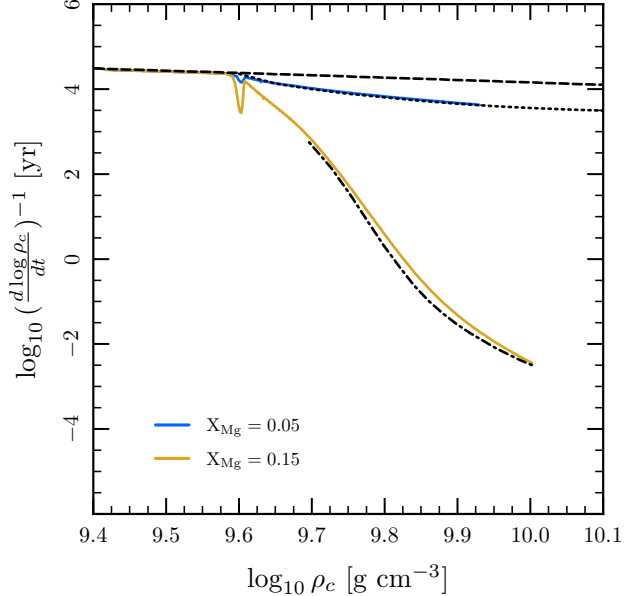


Figure 8. The compression time of selected MESA models. The model with $X_{\text{Mg}} = 0.05$ is compressed at a rate controlled by the accretion rate. The dashed line shows the compression rate given in equation (3) and the dotted line shows the compression rate expected for a zero temperature white dwarf in which Y_e suddenly falls at $\log_{10} \rho = 9.6$, due to the electron captures on ^{24}Mg and ^{24}Na . The agreement demonstrates that the central density is controlled by the total mass. The model with $X_{\text{Mg}} = 0.15$ experiences a much more dramatic decrease in the compression time because of the larger decrease in Y_e (see Fig. 9). The black dash dotted line shows the neutronization timescale expected from the calculations in Appendix D, where the central density is evolving at fixed mass. Note that in both cases the compression timescale still remains orders of magnitude longer than the dynamical time.

at lower central density. These results explain the qualitatively different behavior of the high X_{Mg} models in Fig. 7.

Above the dashed line in Fig. 9, the zero temperature models are dynamically unstable and would contract on the dynamical timescale. But the characteristic electron capture timescales are longer than the dynamical time, and so the assumption that the captures are effectively instantaneous (used in the idealized models in Appendix D) does not hold in the real MESA models. As the contraction timescale gets shorter, only material at densities where the capture timescale is shorter than the contraction timescale can have had significant captures. Therefore the density above which the captures have completed, ρ_n , shifts to higher values. There is no longer time for the total mass to change and so the timescale for the evolution of the central density is no longer set by the accretion rate. Instead, the core compresses on the significantly shorter neutronization timescale,

$$t_n = \left(\frac{d \ln Y_e}{dt} \right)^{-1} = \frac{Y_e A_{\text{Mg}}}{X_{\text{Mg}} \lambda_{\text{ec}}} \approx 80 \left(\frac{X_{\text{Mg}}}{0.15} \right)^{-1} t_{\text{capture}}. \quad (23)$$

Given a fixed M , the models in Appendix D give a relationship between ρ_c and ρ_n . Calculating t_n by evaluating t_{capture} at the ρ_n corresponding to each ρ_c gives the dash dotted line in Fig. 8, which agrees well with the result of the

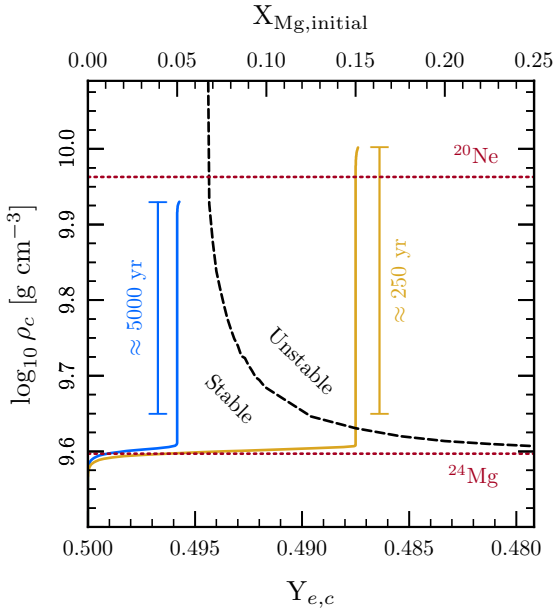


Figure 9. The evolution of the central electron fraction and central density for two values of X_{Mg} (blue and yellow solid lines). The time elapsed during the evolution from $\log_{10} \rho = 9.65$ to the onset of ^{20}Ne captures is indicated next to each track. The dashed line shows the stability curve for a zero temperature white dwarf which neutronizes to the value of $Y_{e,c}$ shown on the x-axis at a density of $\log_{10} \rho = 9.6$. The dotted red lines show the threshold electron capture densities for ^{20}Ne and ^{24}Mg . For $X_{\text{Mg}} \gtrsim 0.07$, the onset of $A = 24$ electron captures reduces Y_e such that subsequent compression drives the equivalent zero temperature models into a dynamically unstable region of parameter space. Past this point, the contraction accelerates significantly (as shown in Fig. 8). In these cases, ^{24}Mg captures alone have assured collapse.

MESA calculation. See Fig. D2 and surrounding discussion for the details of these zero-temperature models.

5.2 Effect of central temperature and accretion rate

As illustrated in Fig. 4, the density at which electron captures begin is temperature dependent. Our fiducial model begins at a central density $\log_{10} \rho_c \approx 9.4$ and $\log_{10} T_c \approx 8.4$. This central temperature is a free parameter, but as discussed in § 3, a new central temperature will be established by the balance between neutrino cooling and compressional heating. Therefore, the central temperature when captures occur (in particular the $A = 20$ captures, and quickly thereafter oxygen ignition) is weakly dependent on the initial temperature. This fact makes it difficult to separately illustrate the effects of the temperature and accretion rate.

In Fig. 10 we show the evolution of our fiducial model with 4 different accretion rates. The onset of captures is less temperature sensitive than one would infer from Fig. 4. This is because at a higher \dot{M} , while the quasi-equilibrium core temperature is higher (increasing the electron capture rates), the compression time is also shorter, and so the density at which $t_{\text{compress}} \approx t_{\text{capture}}$ ends up having a weaker dependence on the accretion rate. At the lowest accretion rate shown in Fig. 10 ($\dot{M} = 10^{-8} M_{\odot} \text{ yr}^{-1}$), the evolution

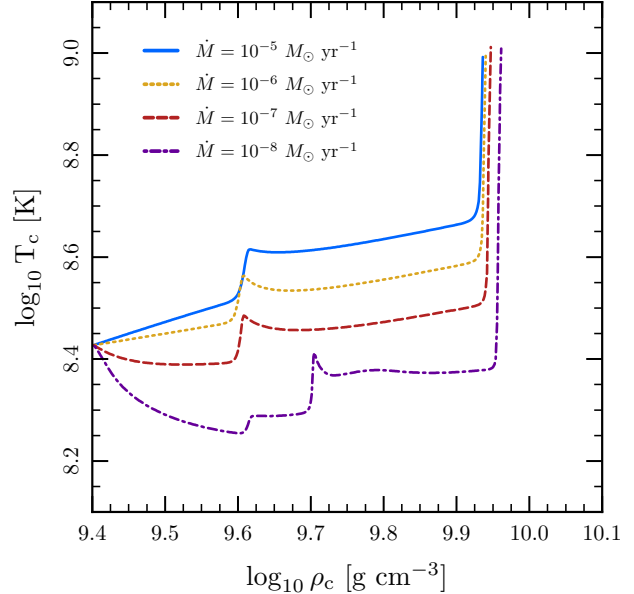


Figure 10. The fiducial model evolved with different values of \dot{M} . The central density at which the $A = 20$ captures occur depends weakly on the accretion rate. At $\dot{M} = 10^{-8} M_{\odot} \text{ yr}^{-1}$ the central temperature remains low enough that the ^{24}Mg and ^{24}Na captures occur at two separate critical densities. The dependence of the oxygen ignition density on \dot{M} is weak.

appears qualitatively different. Looking at Fig. 4, this is because the central temperature remains sufficiently low that electron captures on ^{24}Na do not occur immediately after electron captures on ^{24}Mg , but are delayed until higher densities ($\log_{10} \rho_c \approx 9.7$).

Fig. 11 demonstrates the independence of the oxygen ignition density on the initial central temperature. These models begin right before the $A = 24$ captures, at $\log_{10} \rho_c \approx 9.55$, so that the core temperature does not change substantially before the onset of the captures. By the time the $A = 20$ captures occur, the temperature differences have been erased by neutrino cooling and compressional heating, as the core evolves towards the $t_{\text{compress}} = t_{\text{cool}}$ thermal state discussed in § 3. As a result, there is little effect on the density at which oxygen ignition occurs.

5.3 Effect of a ^{20}Ne forbidden transition

Martínez-Pinedo et al. (2014) discuss the non-unique second forbidden transition from the 0^+ ground state of ^{20}Ne to the 2^+ ground state of ^{20}F . The matrix element for this transition only has an experimental upper limit. They show that this transition can potentially dominate the rate for temperatures less than $9 \times 10^8 \text{ K}$.⁷

⁷ The results of both Martínez-Pinedo et al. (2014) and of this work are obtained by treating the phase space factor of this second forbidden transition as that of an allowed transition. As discussed by Martínez-Pinedo et al. (2014), the true shape factor could contain additional powers of the energy, which would further increase the rate, and can potentially offset the possibility that the matrix element is below the current experimental upper limit.

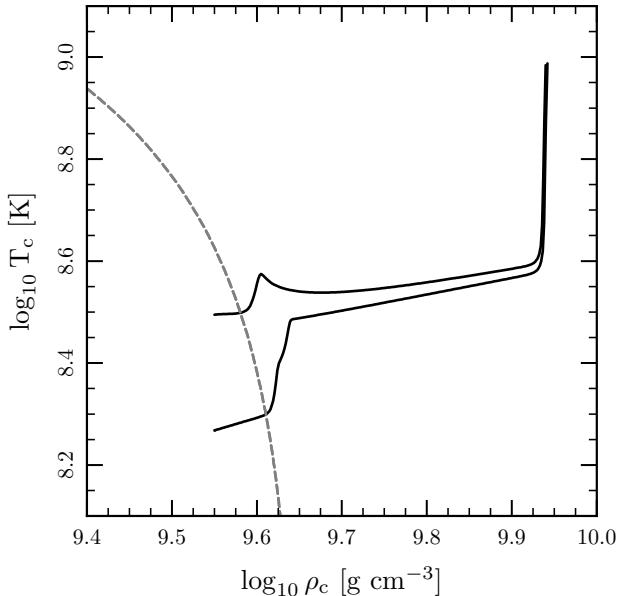


Figure 11. An illustration that the oxygen ignition density is independent of the initial central temperature. The models begin with $\log_{10} \rho_c \approx 9.55$, before the $A = 24$ e-captures. The grey dashed lines show when $t_{\text{capture}} = t_{\text{compress}}$ for ^{24}Mg and the models show the expected temperature dependence for the $A = 24$ captures. However, by the time the $A = 20$ captures occur, the temperature differences have been erased by neutrino cooling and compressional heating, and thus there is little effect on the density at which oxygen ignition occurs.

This transition can affect the critical density at which ^{20}Ne captures begin. The broken lines in Fig. 12 shows the critical curves for ^{20}Ne capture obtained by setting the capture rate equal to the fiducial compression rate, corresponding to $\dot{M} = 10^{-6} M_{\odot} \text{ yr}^{-1}$. With the matrix element at the current experimental upper limit, the onset of captures is shifted to lower density (0.15 dex in $\log_{10} \rho$). At a value a factor of 10^3 below the upper limit, the shift is very approximately halved (depending on the temperature). At a value a factor of 10^6 below the upper limit, the transition ceases to have a substantial effect.

The solid lines in Fig. 12 show the evolution of our fiducial model with each of these different choices for the strength of this transition. While the choice substantially affects the onset of ^{20}Ne captures, it has a less significant effect on the density for oxygen ignition. Unlike the other transitions, which reach the critical capture timescale while they are sub-threshold, this transition is super-threshold. Correspondingly, the electron capture rate is less temperature sensitive. Its less rapid increase, coupled with the compression timescale dropping due to the decrease in Y_e , gives time for the core density to increase before the onset of oxygen ignition.

In the calculation with the transition at the upper limit (solid yellow line), the central temperature does not reach the oxygen ignition line. This is because the thermal structure of the remnant is such that ignition occurs mildly off-center. Our future calculations will determine whether this has any effect on the ensuing evolution.

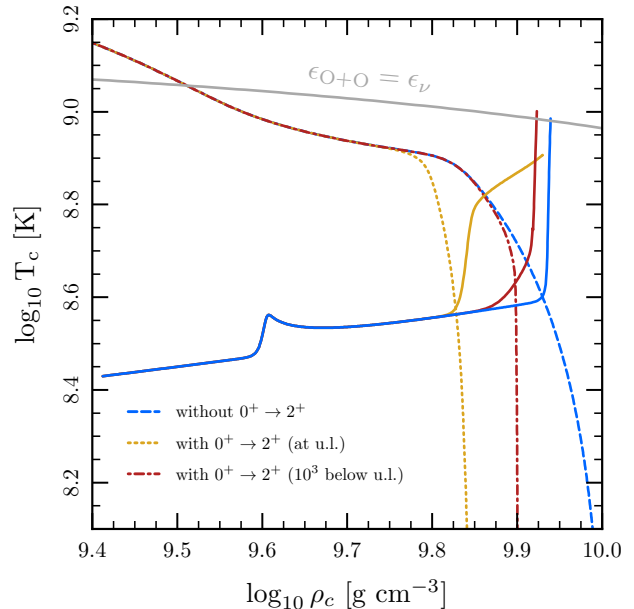


Figure 12. The effect of the second forbidden transition from the 0^+ ground state of ^{20}Ne to the 2^+ ground state of ^{20}F . The dotted, dashed, and dash-dotted lines show where the timescale for ^{20}Ne captures is equal to the fiducial compression timescale (10^4 yr) for different values of the matrix element (see plot legend). The solid lines of matching color show the evolution of the fiducial MESA model using these rates. While the onset of ^{20}Ne captures shifts significantly if the $0^+ \rightarrow 2^+$ transition is at the experimental upper limit, the shift in the density at which oxygen ignition occurs is substantially smaller.

6 DISCUSSION

As described by Miyaji et al. (1980), the final outcome of an ONeMg core as it approaches the Chandrasekhar mass, either explosion or collapse, is determined by a competition between the energy release from the outgoing oxygen deflagration and the energy losses due to electron captures on the post-deflagration material, which has burned to nuclear statistical equilibrium (NSE).

As discussed in § 3, the small length scale of the deflagration means that we are unable to follow this phase with the MESA calculations presented in this paper. However, in lieu of a full calculation, we present a few order-of-magnitude estimates relevant to the outcome.

At the time of collapse, the total energy of our fiducial white dwarf is $E \approx -6 \times 10^{50}$ erg. Oxygen burning to NSE yields approximately 1 MeV per baryon, meaning the energy release from burning $0.3 M_{\odot}$ of material can unbind the white dwarf. This energy release is required for the deflagration wave to significantly change the structure of the star. Prior to the deflagration wave burning through $\approx 0.3 M_{\odot}$ of material, the structure of the WD core will remain relatively unchanged unless electron captures cause collapse. If the deflagration moves at some fraction f of the sound speed, the timescale for it to propagate through the central $0.3 M_{\odot}$ is

$$t_d \approx \int_0^{M_r=0.3M_{\odot}} \frac{dr}{fc_s} \approx 1 \text{ s} \left(\frac{0.03}{f} \right), \quad (24)$$

where we have evaluated the integral using the structure of our MESA model at the end of the calculation.

Nomoto & Kondo (1991) found that the critical deflagration speed that demarcated the boundary between a model that explodes and a model that collapses was $f \approx 0.03$. The work of Timmes & Woosley (1992), which simulated conductively-propagating oxygen deflagrations in detail gives a fitting formula for the laminar deflagration speed of an oxygen flame of

$$v_d = 51.8 \text{ km s}^{-1} \left(\frac{\rho}{6 \times 10^9 \text{ g cm}^{-3}} \right)^{1.06} \left(\frac{X_{\text{O}}}{0.6} \right)^{0.688}. \quad (25)$$

At $\rho \approx 9 \times 10^9 \text{ g cm}^{-3}$ and $X_{\text{O}} = 0.5$, this gives $v_d \approx 70 \text{ km s}^{-1}$, which corresponds to $f = v_d/c_s \approx 0.005$. Based on an analysis of the growth of the Rayleigh-Taylor instability, they conclude that these conductive flames are likely to remain stable. Therefore the laminar flame velocity is representative of the true flame speed in the inner part of the star. In particular, see figure 10 in Timmes & Woosley (1992), noting that $R(M_r = 0.3M_{\odot}) \approx 300 \text{ km}$.

Based on these flame calculations, as well as several KEPLER simulations using these speeds, Timmes & Woosley (1992) concluded that above a core density of $9 \times 10^9 \text{ g cm}^{-3}$ the white dwarfs should collapse to a neutron star. The lowest central density at which oxygen ignition occurred in our parameter study (§ 5) was $\log_{10} \rho_c = 9.93$. That is $\rho_c \approx 8.5 \times 10^9 \text{ g cm}^{-3}$, which is only marginally below this critical value.

The timescale on which the core is neutronizing due to electron captures on the NSE-composition material can be written as $t_n = (d \ln Y_e / dt)^{-1}$. The methods presented in this paper are not appropriate for calculating weak rates in NSE material. Instead, we take \dot{Y}_e from tables generated by Seitenzahl et al. (2009). Fig. 13 shows the neutronization timescale as a function of density and temperature for $Y_e = 0.49$, the approximate central value in our fiducial model at oxygen ignition. Once the deflagration forms, the density of the post-deflagration material is less than the cold, upstream material. The MESA models reach oxygen ignition at $\log_{10} \rho_c \approx 10$, where this density change is small, $\Delta \rho / \rho \approx 0.1$ (Timmes & Woosley 1992). Therefore, the density of the post-deflagration ash will be approximately the same as the density at which oxygen ignites, so Fig. 13 indicates that the relevant neutronization timescale is approximately 0.2 s.

This estimate of the neutronization timescale is sufficiently shorter than the timescale on which the deflagration wave unbinds the star (equation 24) that it suggests that the end result of oxygen ignition following e-captures on ^{20}Ne will be collapse to a NS rather than a thermonuclear explosion. Future work will clarify this in the context of full-star simulations.

7 CONCLUSIONS

We have provided an updated analytic and numerical understanding of the evolution of accreting and compressing ONeMg cores up to the initiation of oxygen burning in the core. This study was enabled by new capabilities of the MESA (Paxton et al. 2011, 2013, 2015) stellar evolution code. In particular, we have implemented a highly accurate

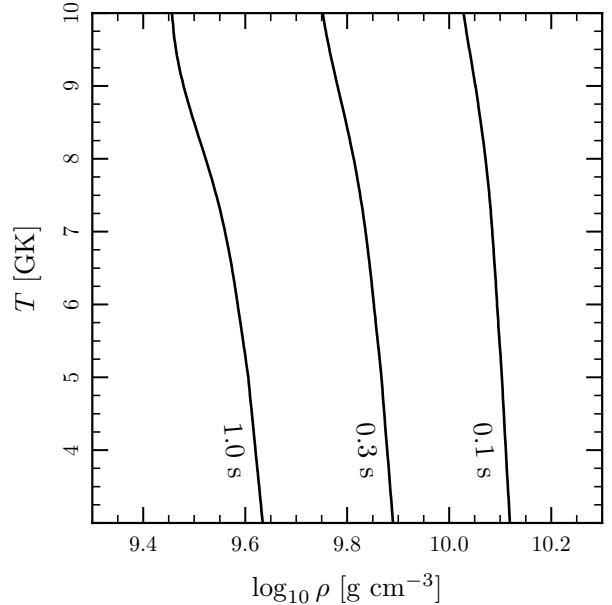


Figure 13. The neutronization timescale for $Y_e = 0.49$, which is roughly the central value of Y_e at the end of our fiducial calculation. Contours are labeled by timescale. This uses the NSE electron capture rates from Seitenzahl et al. (2009). Since our compressing ONeMg cores reach oxygen ignition at $\log_{10} \rho_c \approx 10$, the relevant neutronization timescale is approximately 0.2 s. This is less than the timescale for the O deflagration wave to release enough energy to unbind the star (equation 24), suggesting that collapse to a NS will ensue.

treatment of the key electron capture rates (on $A = 20$ and 24 nuclei) using modern microphysics from Martínez-Pinedo et al. (2014), which is summarized in Appendix A.

We have demonstrated analytically and numerically that neither ^{24}Mg or ^{20}Ne captures release sufficient heat to generate convection in the core. Instead, the core undergoes a thermal runaway triggered by the energy released by ^{20}Ne captures. This centrally concentrated runaway initiates oxygen burning and launches an outgoing oxygen deflagration wave at a time when the central density is at least $8.5 \times 10^9 \text{ g cm}^{-3}$. Based on order of magnitude estimates and previous work of Timmes & Woosley (1992), we expect objects which ignite oxygen at such high densities will collapse and form a neutron star due to continued electron captures on the NSE ashes produced by oxygen burning.

Given the sensitivity of the final outcome of compressing ONeMg cores to the central density at the time oxygen burning begins (see §6), we also performed a parameter study which demonstrated the influence of a number of factors on this density. We investigated the effects of varying the initial ^{24}Mg fraction (§ 5.1), the initial central temperature and accretion rate (§ 5.2), as well as the potential inclusion of a particular forbidden transition (§ 5.3). Figures 8 and 9 demonstrate that values of $X_{\text{Mg}} \gtrsim 0.07$ cause the core to contract more rapidly after $A = 24$ the captures, which leads to oxygen ignition at higher densities (thus further favoring collapse to form a neutron star). We also demonstrated the importance of the balance between neutrino cooling and compressional heating in setting the

central temperature of ONeMg cores during much of their evolution (Paczynski 1971). This implies that the core typically loses memory of its initial central temperature.

The approach of an ONeMg core to the Chandrasekhar mass is relevant to the late stages of evolution for super asymptotic giant branch stars, binary systems with an accreting ONeMg WD, and the remnants of WD-WD mergers. Our calculations here are an important step in producing more realistic progenitor models for these studies.

ACKNOWLEDGMENTS

We thank Gabriel Martínez-Pinedo and Christopher Sullivan for discussing their work in Martínez-Pinedo et al. (2014) with us in advance of publication. We thank Jared Brooks, Dan Kasen, Christian Ott, Sterl Phinney and Ken Shen for useful discussions. We thank Frank Timmes for his comments on the manuscript. We acknowledge stimulating workshops at Sky House where these ideas germinated. JS is supported by the National Science Foundation Graduate Research Fellowship Program under Grant No. DGE 1106400 and by NSF grant AST-1205732. EQ is supported in part by a Simons Investigator award from the Simons Foundation and the David and Lucile Packard Foundation. LB is supported by the National Science Foundation under grants PHY 11-25915, AST 11-09174, and AST 12-05574. This research used the SAVIO computational cluster resource provided by the Berkeley Research Computing program at the University of California Berkeley (Supported by UC Chancellor, UC Berkeley Vice Chancellor of Research and Office of the CIO). This research has made use of NASA's Astrophysics Data System.

REFERENCES

- Aparicio J. M., 1998, *ApJS*, 117, 627
 Canal R., Isern J., Labay J., 1992, *ApJ*, 398, L49
 Chabrier G., Potekhin A. Y., 1998, *Phys. Rev. E*, 58, 4941
 Commins E., 1973, *Weak Interactions*. McGraw-Hill
 Couch R. G., Loumos G. L., 1974, *ApJ*, 194, 385
 Cox J. P., 1968, *Principles of stellar structure - Vol.1: Physical principles; Vol.2: Applications to stars*
 Dewitt H. E., Graboske H. C., Cooper M. S., 1973, *ApJ*, 181, 439
 Farmer R., Fields C. E., Timmes F. X., 2015, *ApJ*, 807, 184
 Firestone R. B., 2007, *Nuclear Data Sheets*, 108, 2319
 Fuller G. M., Fowler W. A., Newman M. J., 1980, *ApJS*, 42, 447
 Fuller G. M., Fowler W. A., Newman M. J., 1985, *ApJ*, 293, 1
 Gove N. B., Martin M. J., 1971, *Atomic Data and Nuclear Data Tables*, 10, 205
 Gutiérrez J., Canal R., García-Berro E., 2005, *A&A*, 435, 231
 Gutierrez J., Garcia-Berro E., Iben Jr. I., Isern J., Labay J., Canal R., 1996, *ApJ*, 459, 701
 Ichimaru S., 1993, *Reviews of Modern Physics*, 65, 255
 Isern J., Canal R., Labay J., 1991, *ApJ*, 372, L83
 Itoh N., Tomizawa N., Tamamura M., Wanajo S., Nozawa S., 2002, *ApJ*, 579, 380
 Jones S., Hirschi R., Nomoto K., 2014, *ApJ*, 797, 83
 Jones S., Hirschi R., Nomoto K., Fischer T., Timmes F. X., Herwig F., Paxton B., Toki H., Suzuki T., Martínez-Pinedo G., Lam Y. H., Bertolli M. G., 2013, *ApJ*, 772, 150
 Juodagalvis A., Langanke K., Hix W. R., Martínez-Pinedo G., Sampaio J. M., 2010, *Nuclear Physics A*, 848, 454
 Langer N., 1991, *A&A*, 252, 669
 Langer N., Fricke K. J., Sugimoto D., 1983, *A&A*, 126, 207
 Martínez-Pinedo G., Lam Y. H., Langanke K., Zegers R. G. T., Sullivan C., 2014, *Phys. Rev. C*, 89, 045806
 Miyaji S., Nomoto K., 1987, *ApJ*, 318, 307
 Miyaji S., Nomoto K., Yokoi K., Sugimoto D., 1980, *PASJ*, 32, 303
 Nomoto K., 1984, *ApJ*, 277, 791
 Nomoto K., Kondo Y., 1991, *ApJ*, 367, L19
 Oda T., Hino M., Muto K., Takahara M., Sato K., 1994, *Atomic Data and Nuclear Data Tables*, 56, 231
 Paczyński B., 1971, *Acta Astron.*, 21, 271
 Paxton B., Bildsten L., Dotter A., Herwig F., Lesaffre P., Timmes F., 2011, *ApJS*, 192, 3
 Paxton B., Cantiello M., Arras P., Bildsten L., Brown E. F., Dotter A., Mankovich C., Montgomery M. H., Stello D., Timmes F. X., Townsend R., 2013, *ApJS*, 208, 4
 Paxton B., Marchant P., Schwab J., Bauer E. B., Bildsten L., Cantiello M., Dessart L., Farmer R., Hu H., Langer N., Townsend R. H. D., Townsley D. M., Timmes F. X., 2015, *ArXiv e-prints*
 Potekhin A. Y., Chabrier G., 2000, *Phys. Rev. E*, 62, 8554
 Potekhin A. Y., Chabrier G., Rogers F. J., 2009, *Phys. Rev. E*, 79, 016411
 Ritossa C., García-Berro E., Iben Jr. I., 1999, *ApJ*, 515, 381
 Saio H., Nomoto K., 1985, *A&A*, 150, L21
 Schwab J., Shen K. J., Quataert E., Dan M., Rosswog S., 2012, *MNRAS*, 427, 190
 Seitenzahl I. R., Townsley D. M., Peng F., Truran J. W., 2009, *Atomic Data and Nuclear Data Tables*, 95, 96
 Shapiro S. L., Teukolsky S. A., 1983, *Black holes, white dwarfs, and neutron stars: The physics of compact objects*
 Shen K. J., Bildsten L., Kasen D., Quataert E., 2012, *ApJ*, 748, 35
 Takahara M., Hino M., Oda T., Muto K., Wolters A. A., Glaudemans P. W. M., Sato K., 1989, *Nuclear Physics A*, 504, 167
 Takahashi K., Yoshida T., Umeda H., 2013, *ApJ*, 771, 28
 Tilley D. R., Cheves C. M., Kelley J. H., Raman S., Weller H. R., 1998, *Nuclear Physics A*, 636, 249
 Timmes F. X., Swesty F. D., 2000, *ApJS*, 126, 501
 Timmes F. X., Woosley S. E., 1992, *ApJ*, 396, 649
 Yakovlev D. G., Shalybkov D. A., 1989, *Astrophysics and Space Physics Reviews*, 7, 311
 Yoon S.-C., Langer N., Norman C., 2006, *A&A*, 460, 199

APPENDIX A: PHYSICS OF ELECTRON-CAPTURE AND BETA-DECAY

We are interested in the electron-capture reaction

$$(Z, N) + e^- \rightarrow (Z - 1, N + 1) + \nu_e \quad (\text{A1})$$

and its reverse reaction, β -decay

$$(Z, N) \rightarrow (Z + 1, N - 1) + e^- + \bar{\nu}_e \quad (\text{A2})$$

where Z and N are respectively the proton and neutron number of the nucleus. For nuclei in a dense plasma where the electrons are degenerate, the rates of these processes can depend sensitively on the density (though the electron distribution function) and temperature (though the occupation of nuclear energy levels and the electron distribution function). The neutrinos are able to free stream out of the star, and therefore neutrino phase-space is effectively unfilled. For a more thorough discussion of the physics of weak reactions in stellar environments, see e.g. Fuller et al. (1980, 1985).

This section summarizes a simple framework for the rates of these weak processes. More detailed microscopic calculations exist in the literature such as those presented in Oda et al. (1994). However, those particular tables are sufficiently sparse that numerical considerations related to interpolation cause us to elect to use rates calculated in the manner described here, rather than interpolate in tables from more detailed calculations.

The rate of the electron capture or β -decay transition from the i -th state of the parent nucleus to the j -th state of the daughter nucleus can be written as (e.g. Fuller et al. 1980)

$$\lambda_{ij} = \frac{\ln 2}{(ft)_{ij}} I(\mu, T, Q_{ij}), \quad (\text{A3})$$

where (ft) is the comparative half-life and can be either measured experimentally or theoretically calculated from the weak-interaction nuclear matrix elements. I is a phase space factor which depends on the temperature T , electron chemical potential μ , and the energy difference Q_{ij} between the (i -th) parent and (j -th) daughter nuclear states.

$$Q_{ij} = (\mu_p - \mu_d) + E_i - E_j, \quad (\text{A4})$$

where μ_p and μ_d are the chemical potentials of the nuclei. For a classical ideal gas, the chemical potential is

$$\mu_I = m_I c^2 + kT \ln \left(\frac{n_I}{n_q} \right), \quad (\text{A5})$$

where m_I is the rest mass, n_I is the number density, and $n_q = (2\pi m_I kT/h^2)^{3/2}$. Therefore,

$$Q_{ij} = (M_p - M_d) c^2 + kT \ln \left(\frac{n_p}{n_d} \right) + E_i - E_j \quad (\text{A6})$$

where M_p and M_d are the nuclear rest masses of the parent and daughter nuclei, respectively. Since $|M_p - M_d| c^2 \approx 5$ MeV for the isotopes we consider and we restrict ourselves to temperatures $T < 10^9$ K (so $kT < 100$ keV), the term $kT \ln \left(\frac{n_p}{n_d} \right)$ is negligible in comparison and we discard it, leaving

$$Q_{ij} = (M_p - M_d) c^2 + E_i - E_j. \quad (\text{A7})$$

Though not generally true, for the set of transitions that we

consider, this definition means that $Q_{ij} < 0$ for e-capture and $Q_{ij} > 0$ for β -decay.

We work in the allowed approximation, which neglects all total lepton angular momentum ($L = 0$). This restricts us to the following transitions and corresponding selection rules (e.g. Commins 1973): Fermi transitions, where the total lepton spin is $S = 0$, and therefore the initial and final nuclear spins are equal ($J_i = J_j$), and Gamow-Teller transitions, where $S = 1$, and therefore $J_i = J_j, J_j \pm 1$ (excluding $J_i = J_f = 0$). In both cases, there is no parity change: $\pi_i \pi_f = +1$.

At low temperature, the electron chemical potential is approximately the Fermi energy E_F (the first correction enters at order $(kT/E_F)^2$), and so we use the terms Fermi energy and chemical potential interchangeably. In the relativistic limit, the chemical potential can be approximated as

$$\mu \approx E_F = 5.16 \left(\frac{\rho Y_e}{10^9 \text{g cm}^{-3}} \right)^{1/3} \text{ MeV}, \quad (\text{A8})$$

where $Y_e = \sum_i Z_i X_i / A_i$ is the electron fraction. Z_i , X_i , and A_i are respectively the charge, mass fraction, and atomic mass of the i -th species.

The total rate of the process is the sum of the individual transition rates from the i -th parent state to the j -th daughter state, λ_{ij} , weighted by the occupation probability of the i -th parent state, p_i .

$$\lambda_{\text{total}} = \sum_i p_i \sum_j \lambda_{ij}, \quad (\text{A9})$$

The i -sum is over all parent states and the j -sum is over all daughter states. We will always assume that the nuclear states are populated with a thermal (Boltzmann) distribution. Some parent nuclei preferentially capture into excited daughter states, but these excited states decay via γ -ray emission with a typical timescale $\sim 10^{-12}$ s. Therefore the level population returns to a thermal distribution on a timescale much shorter than the evolutionary timescales of interest.⁸ The occupation probability is

$$p_i = \frac{2J_i + 1}{P(T)} \exp(-\beta E_i), \quad (\text{A10})$$

where $P(T)$, the nuclear partition function is $P(T) = \sum_i (2J_i + 1) e^{-\beta E_i}$ and we define $\beta = (kT)^{-1}$.

The remainder of this section considers the rate of a single allowed ($L = 0$) transition in detail, and so for convenience we drop the i, j subscripts. In the case of electron

⁸ There is one case in which this hierarchy of timescales is not so obvious. The first excited state of ^{24}Na is metastable with a half-life of 2×10^{-2} s (Firestone 2007) and ground state of ^{24}Mg preferentially captures into this excited state. If the capture rate from this excited state to ^{24}Ne were approximately equal or greater than the rate of decay via γ -ray emission, the relative state populations would be effectively non-thermal. Using the parameters of this transition as listed in Table 1, the capture timescale is approximately equal to the half-life at a critical density of $\log_{10} \rho \approx 10.5$ (for $Y_e \approx 0.5$), which is safely outside of the density range that we consider in this work.

capture, the phase space factor is (e.g., Fuller et al. 1980)

$$I_{ec} = \frac{1}{(m_e c^2)^5} \int_{-Q}^{\infty} \frac{E_e^2 E_\nu^2}{1 + \exp[\beta(E_e - \mu)]} G(Z, E_e) dE_e, \quad (\text{A11})$$

along with the energy conservation relationship $E_e + Q = E_\nu$. The quantity G is defined as

$$G(Z, E_e) = \frac{\sqrt{E_e^2 - (m_e c^2)^2}}{E_e} F(Z, E_e) \quad (\text{A12})$$

where $F(Z, E_e)$ is the relativistic Coulomb barrier factor (Gove & Martin 1971). We make the approximation that the electrons are relativistic. In this limit,

$$G(Z, E_e) \approx \left(\frac{4\pi E_e R}{hc} \right)^{-\alpha^2 Z^2} \exp(\pi\alpha Z), \quad (\text{A13})$$

where α is the fine structure constant and R is the size of the nucleus (Fuller et al. 1980). We are considering nuclei with $Z \approx 10$, $A \approx 20$ (and so $R \approx 3$ fm), at densities such that $E_e \approx 5$ MeV. Therefore, the value of the first term is $(\frac{4\pi E_e R}{hc})^{-\alpha^2 Z^2} \approx 0.999$, with an extremely weak E_e and R dependence (since $\alpha^2 Z^2 \approx 0.005$). Therefore we treat $G(Z, E_e)$ as a constant with a value of $\exp(\pi\alpha Z)$.

Changing to dimensionless variables $\epsilon \equiv \frac{E}{m_e c^2}$ and $q \equiv \frac{Q}{m_e c^2}$, the phase space integral becomes

$$I_{ec} = e^{\pi\alpha Z} \int_{-q}^{\infty} \frac{\epsilon^2(\epsilon + q)^2}{1 + \exp[\beta m_e c^2(\epsilon - \mu)]} d\epsilon. \quad (\text{A14})$$

We rewrite this integral in simpler form as

$$I_{ec} = \frac{e^{\pi\alpha Z}}{(\beta m_e c^2)^5} [F_4(\eta + \zeta) - 2\zeta F_3(\eta + \zeta) + \zeta^2 F_2(\eta + \zeta)], \quad (\text{A15})$$

where we have defined the quantities $\eta = \beta\mu$ and $\zeta = \beta q$ and

$$F_k(y) = \int_0^{\infty} \frac{x^k}{1 + \exp(x - y)} dx, \quad (\text{A16})$$

is the complete Fermi integral. Evaluating the rate requires evaluating three complete Fermi integrals, for which efficient numerical routines exist (e.g. Aparicio 1998).

In addition to the e-capture rate, we need the rate of energy loss via neutrinos, which for a single transition can be written as

$$\varepsilon_{\nu, ij} = \frac{m_e c^2 \ln 2}{(ft)_{ij}} J(\mu, T, Q_{ij}), \quad (\text{A17})$$

where J is phase space factor, defined by an integral similar to equation (A11), except with an additional power of the neutrino energy:

$$J_{ec} = \frac{1}{(m_e c^2)^6} \int_{-Q}^{\infty} \frac{E_e^2 E_\nu^3}{1 + \exp[\beta(E_e - \mu)]} G(Z, E_e) dE_e. \quad (\text{A18})$$

In terms of complete Fermi integrals, this is

$$J_{ec} = \frac{e^{\pi\alpha Z}}{(\beta m_e c^2)^6} [F_5(\eta + \zeta) - 2\zeta F_4(\eta + \zeta) + \zeta^2 F_3(\eta + \zeta)]. \quad (\text{A19})$$

The total neutrino loss rate can be calculated via an occupation-weighted average, analogous to that used to calculate the total rate in equation (A9).

In the case of β -decay, the phase space factor is

$$I_\beta = \int_{m_e c^2}^Q \frac{E_e^2 E_\nu^2}{1 + \exp[-\beta(E - \mu)]} G(Z, E) dE_e, \quad (\text{A20})$$

and energy conservation $Q = E_e + E_\nu$. Following the same procedure as the electron capture case⁹

$$I_\beta = e^{\pi\alpha Z} \int_1^q \frac{\epsilon^2(\epsilon - q)^2}{1 + \exp[-\beta m_e c^2(\epsilon - \mu)]} d\epsilon. \quad (\text{A21})$$

We can convert this integral into a sum of complete Fermi integrals by making use of the mathematical identity

$$\int_0^b \frac{x^k}{1 + \exp(x - y)} = F_k(y) - \sum_{j=0}^k \binom{k}{j} b^{k-j} F_j(y - b). \quad (\text{A22})$$

Defining $\vartheta \equiv \beta m_e c^2$, this yields the following expression:

$$\begin{aligned} I_\beta = & \frac{e^{\pi\alpha Z}}{(\beta m_e c^2)^5} [F_4(\zeta - \eta) - 2\zeta F_3(\zeta - \eta) + \zeta^2 F_2(\zeta - \eta)] - \\ & \frac{e^{\pi\alpha Z}}{(\beta m_e c^2)^5} [F_4(\vartheta - \eta) - \\ & F_3(\vartheta - \eta) \times (4\vartheta - 2\zeta) + \\ & F_2(\vartheta - \eta) \times (6\vartheta^2 - 6\vartheta\zeta + \zeta^2) - \\ & F_1(\vartheta - \eta) \times (4\vartheta^3 - 6\vartheta^2\zeta + 2\vartheta\zeta^2) + \\ & F_0(\vartheta - \eta) \times (\vartheta^4 - 2\vartheta^3\zeta + \vartheta^2\zeta^2)]. \end{aligned} \quad (\text{A23})$$

Similarly, the factor J_β necessary to calculate the neutrino loss rate is

$$J_\beta = \int_{m_e c^2}^Q \frac{E_e^2 E_\nu^3}{1 + \exp[-\beta(E - \mu)]} G(Z, E) dE_e, \quad (\text{A24})$$

which can be written as

$$\begin{aligned} J_\beta = & \frac{e^{\pi\alpha Z}}{(\beta m_e c^2)^6} [F_5(\zeta - \eta) - 2\zeta F_4(\zeta - \eta) + \zeta^2 F_3(\zeta - \eta)] - \\ & \frac{e^{\pi\alpha Z}}{(\beta m_e c^2)^6} [F_5(\vartheta - \eta) - \\ & F_4(\vartheta - \eta) \times (5\vartheta - 3\zeta) + \\ & F_3(\vartheta - \eta) \times (10\vartheta^2 - 12\vartheta\zeta + 3\zeta^2) - \\ & F_2(\vartheta - \eta) \times (10\vartheta^3 - 18\vartheta^2\zeta + 9\vartheta\zeta^2 - \zeta^3) + \\ & F_1(\vartheta - \eta) \times (5\vartheta^4 - 12\vartheta^3\zeta + 9\vartheta^2\zeta^2 - 2\vartheta\zeta^3) - \\ & F_0(\vartheta - \eta) \times (\vartheta^5 - 3\vartheta^4\zeta + 3\vartheta^3\zeta^2 - \vartheta^2\zeta^3)]. \end{aligned} \quad (\text{A25})$$

Given the reaction rates and neutrino energy loss rates, we can calculate the net heating rate of the plasma. The energy equation for material in the star is

$$T \frac{ds}{dt} = -\frac{\partial L}{\partial M} + q_* + q_{ec} + q_\beta \quad (\text{A26})$$

where q_{ec} and q_β account for the set of weak nuclear reactions we are considering separately and q_* includes all other

⁹ It is perhaps less obvious that the assumption that the electrons are relativistic is justified here, given the lower integration limit. But because electron phase space is only empty near or above the Fermi energy (and $\mu > 5$ MeV at the densities of interest), the integrand is only significant at the upper portion of the integration range where this approximation is justified.

heating and cooling sources such as thermal neutrino losses and other nuclear reactions. Under the assumption of thermal equilibrium, the energy released by the weak reactions depends only on the total reaction rate, the total neutrino loss rate, and the ion and electron chemical potentials. The energy generation rate (per capture or decay) is

$$\varepsilon_{ec} = (-\mu_{I,Z} + \mu_{I,Z-1} + \mu_e)\lambda_{ec} - \varepsilon_{\nu,ec} \quad (\text{A27})$$

$$\varepsilon_{\beta} = (-\mu_{I,Z-1} + \mu_{I,Z} - \mu_e)\lambda_{\beta} - \varepsilon_{\nu,\beta} \quad (\text{A28})$$

where $\mu_{I,Z}$, $\mu_{I,Z-1}$ are the chemical potentials of the ions with those charges and μ_e is the chemical potential of the electron. Defining $Q_g \equiv Q_{00} = (M_p - M_d)c^2$, which implicitly making the same assumption used to derive equation (A7), the specific energy generation rates are

$$q_{ec} = \frac{n_{ec}}{\rho} \varepsilon_{ec} = \frac{n_{ec}}{\rho} [(Q_g + \mu_e)\lambda_{ec} - \varepsilon_{\nu,ec}] , \quad (\text{A29})$$

$$q_{\beta} = \frac{n_{\beta}}{\rho} \varepsilon_{\beta} = \frac{n_{\beta}}{\rho} [(Q_g - \mu_e)\lambda_{\beta} - \varepsilon_{\nu,\beta}] , \quad (\text{A30})$$

where n_{ec} and n_{β} are the number densities of the species undergoing capture and decay. Therefore, given a list of nuclear levels and the (*ft*)-values for the transitions between them, we can calculate the rates of and energy generation rates from electron-capture and β -decay.

Using the above approach, it would be possible to generate tables whose points are spaced sufficiently closely, such that interpolation would no longer incur significant errors. But because MESA comes with fast quadrature routines to evaluate equation (A16), it directly evaluates equations (A15), (A19), (A23), and (A25) each time one of the weak reaction rates is needed. While this is computationally inefficient, the overall speed of our calculations is sufficiently unaffected that we chose not to optimize this.

APPENDIX B: COULOMB CORRECTIONS

In a dense plasma, the electrostatic interactions of the ions and electrons introduce corrections to the weak rates relative to rates which assume a Fermi gas of electrons and an ideal gas of ions (as do those presented in Appendix A). The leading term in the Coulomb interaction energy for ion-ion interactions (e.g. Shapiro & Teukolsky 1983) is

$$E_c = -\frac{9}{10} \frac{Z^2 e^2}{a_i} \quad (\text{B1})$$

where $a_i = \left(\frac{3}{4\pi n_i}\right)^{1/3}$ is the inter-ionic spacing. For $Z \approx 10$, $E_c \approx -0.2E_F$ indicating that the interactions are energetically important.¹⁰

In this section, we discuss our treatment of these corrections, and compare our approach to previous work. Our treatment is most similar to that discussed in Appendix A of Juodagalvis et al. (2010). Fig. B1 illustrates the effects of including these corrections on the evolution of our fiducial model. The change in the evolution is similar to that observed by Gutierrez et al. (1996).

¹⁰ The Coulomb interaction energy and the Fermi energy both scale $\propto \rho^{1/3}$ in the relativistic limit.

B1 Equation of State

Most straightforwardly, a Coulomb term appears in the ion equation of state. This affects the weak reaction rates, because at a fixed total pressure the electron density is lower. The MESA equation of state routines, which in the thermodynamic regime of interest are based on the Helmholtz equation of state (Timmes & Swesty 2000), include these terms based on the work of Yakovlev & Shalybkov (1989).

B2 Ion Chemical Potential

The energy required to remove an ion of one species and create an ion of another species is given by the difference in the ion chemical potentials. Since electron-capture and beta-decay change the ion charge, the presence of the Coulomb interaction energy changes the energy difference between the parent and daughter nuclear states. The interaction energy is negative, and so decreasing the charge of the nucleus (as electron-capture reactions do) requires additional energy, which will therefore shift the onset of electron captures to higher density.

To calculate this shift, we use the excess (that is, the part in addition to the ideal contribution) ion chemical potential μ_{ex} developed in the following series of papers: Chabrier & Potekhin (1998); Potekhin & Chabrier (2000); Potekhin et al. (2009). We incorporate this effect by shifting the value of Q , as defined in equation (A4), by an amount $\Delta E = \mu_{ex,p} - \mu_{ex,d}$. This shift,

$$Q' = Q + \Delta E \quad (\text{B2})$$

then enters the calculation of the phase space factors and the energy generation rates. In Fig. B1, the red dotted line labeled “ion chemical potential”, shows the effect of including of these corrections.

B3 Screening

The electron density relevant to the reaction rate is not the average electron density, but rather the electron density at the position of the nucleus. Itoh et al. (2002) calculated the value of this screening correction using linear response theory. This correction can be correctly accounted for as a shift in the value of the electron chemical potential that enters the phase space factor.

$$\mu'_e = \mu_e + V_s \quad (\text{B3})$$

However, this correction does not enter the energy generation rates because it has not changed the energy cost to add or remove an electron from the bulk Fermi sea, which is the net effect of a capture or decay. In Fig. B1, the yellow dashed line labeled “electron screening”, shows the effect of including these corrections.

B4 Comparison with Previous Work

The effect discussed in §B2, which is the dominant Coulomb correction, has previously been included in studies of ONeMg cores (e.g. Gutierrez et al. 1996; Takahashi et al. 2013). The approach taken in these studies is to include this effect as a shift in the *electron* chemical potential

$$\mu'_e = \mu_e - \Delta E \quad (\text{B4})$$

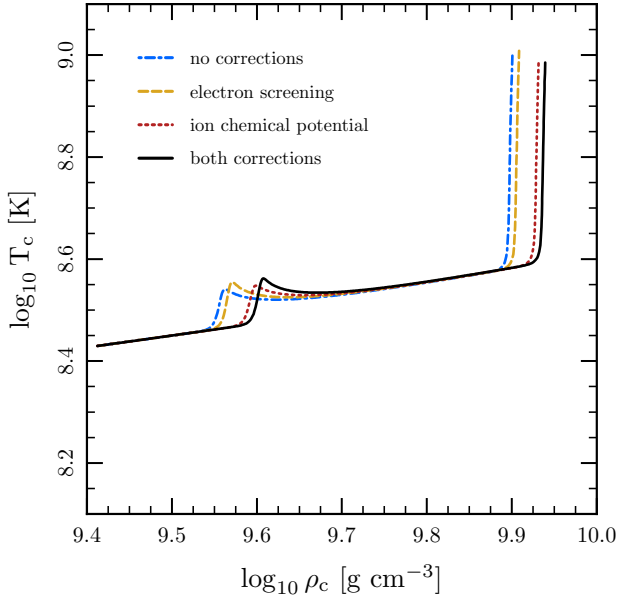


Figure B1. Illustration of the effect of Coulomb corrections on the evolution of the central density and temperature of the accreting core. (To better understand this plot the reader may first want to consult Fig. 3 and the surrounding discussion.) All calculations include the corrections to the equation of state (§ B1). The dashed-dotted blue line shows the result with no other corrections. The dashed yellow line shows the effect of the inclusion of the screening corrections (§ B3). The dotted red line shows the effect of the inclusion of the corrections to the ion chemical potential (§ B2). The solid black line shows the result with both corrections included, which is the default choice for our calculations. The primary effect of including these corrections is a increase (of about 0.05 dex) in the density at which electron captures occur.

and to use this modified electron chemical potential in the evaluation of the rates. This approach is conceptually incorrect, because μ_e and Q enter the rate expression in different ways, as can be seen in equation (A11). However, given a table of $\lambda_{ec}(\rho, T)$, one has no ability to shift Q , so the only way to correct the rate is to shift the relation between μ_e and ρ . In the sub-threshold case (see equation 6), the most important term is the exponential, which *is* symmetric in Q and μ , and so this approach does not lead to a substantial quantitative error in the rate.

When making this correction both Gutierrez et al. (1996) and Takahashi et al. (2013) follow Couch & Loumos (1974) and use the form of the ion free energy from Dewitt et al. (1973). There has been progress in calculating the free energy of electron-ion plasmas in the last few decades. As discussed in § B2, we use the fitting formula for the free energy from Potekhin et al. (2009). In their work on electron capture rates in NSE material, Juodagalvis et al. (2010) use the formula quoted in Ichimaru (1993). The results of Ichimaru (1993) and Potekhin et al. (2009) agree, while the shift calculated following Dewitt et al. (1973) is approximately 30 per cent larger in magnitude.

The screening correction discussed in § B3 is not as widely adopted. It is included in Juodagalvis et al. (2010), but not in Gutierrez et al. (1996). The results of Itoh et al. (2002) are within approximately 10 per cent of the results

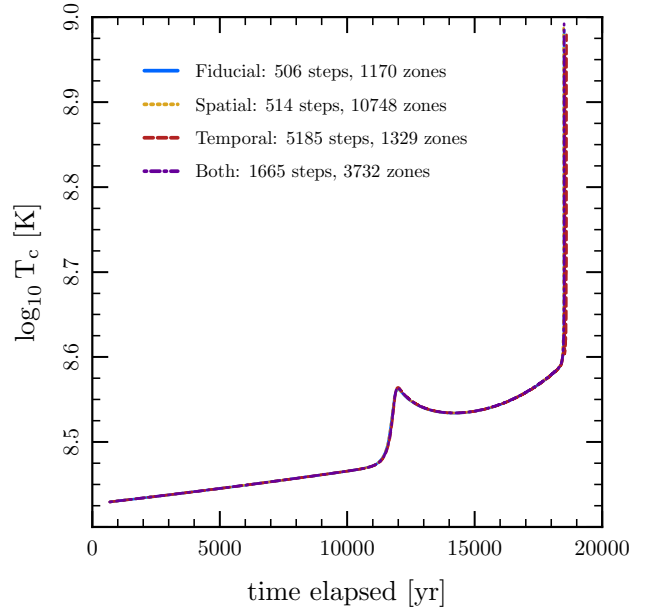


Figure C1. The legend shows the number of timesteps and the maximum number of zones used in the calculation of each of the runs shown in Table C. The negligible variation between models indicates our results are converged.

from the Thomas-Fermi approximation

$$V_s \approx Z \sqrt{\frac{4\alpha^3}{\pi}} E_F. \quad (\text{B5})$$

This effect has approximately the magnitude of the difference between older ion chemical potential and the one we adopt discussed in the preceding paragraph, but the opposite sign. Therefore, despite its exclusion, the net difference between our calculations and those of Gutierrez et al. (1996) is small.

APPENDIX C: CONVERGENCE

In order to demonstrate that our results are robust, we perform a number of tests of the spatial and temporal convergence of our MESA calculations. The parameters of these runs are shown in Table C. We performed runs with each of the spatial and temporal resolutions each separately ten times greater than the fiducial case, as well as a run in which both the spatial and temporal resolutions were three times greater than the fiducial case. Fig. C1 shows that the central temperature evolution remains unchanged¹¹ and we observed that the variation of the result in any quantity of interest was negligible.

In addition, we performed a run with a much larger network (203 isotopes; `mesa_201.net` plus ^{20}O and ^{20}F) and confirmed that our results remained unchanged.

¹¹ The small difference at the end of the “Temporal” track is an artifact of a difference in how the stopping condition trigger was tripped.

Run Name	<code>delta_lgRho_cntr_limit</code>	<code>delta_lgRho_cntr_hard_limit</code>	<code>varcontrol_target</code>	<code>mesh_delta_coeff</code>
Fiducial	1×10^{-3}	3×10^{-3}	1×10^{-3}	1.0
Temporal	1×10^{-4}	3×10^{-4}	1×10^{-4}	–
Spatial	–	–	–	0.1
Both	3×10^{-4}	1×10^{-3}	3×10^{-4}	0.3

Table C1. Parameters for the runs demonstrating the convergence of our results. The column names are the specific MESA controls we used. The controls `delta_lgRho_cntr_limit`, `delta_lgRho_cntr_hard_limit`, `varcontrol_target` control the maximal fractional change in physical variables, which in an implicit code like MESA controls the timestep. The control `mesh_delta_coeff` controls the number of zones used in the calculation. Fig. C1 shows that central temperature evolution is essentially identical for these different runs.

APPENDIX D: TWO-ZONE WD MODELS

This section describes the framework we use to understand the evolution of our MESA models after the $A = 24$ captures have occurred. The quantitative estimates shown in Figs. 8 and 9 were made using the approach described in this Appendix.

After the $A = 24$ electron captures have begun in the center of the WD, the MESA models have two zones: an inner “neutronized” zone in which the captures have occurred and Y_e is lower, and an outer zone whose composition remains unchanged. This property of our MESA models can be seen in Fig. 5. The neutronized zone is growing (in a Lagrangian sense) as a function of time.

In § D1 we write down an idealized model of a white dwarf with this two zone structure. In § D2 we discuss how we apply these models to understand our MESA calculations.

D1 Details of the Two-Zone Model

Following Cox (1968), we write down a simple model of a zero-temperature white dwarf. We assume spherical symmetry and hydrostatic equilibrium and so solve the Poisson equation in spherical coordinates:

$$\frac{1}{r^2} \frac{d}{dr} \left(r^2 \frac{dP}{dr} \right) = -4\pi G \rho. \quad (\text{D1})$$

We also assume the equation of state of a zero temperature, ideal Fermi gas, which is

$$P = Af(x) \quad (\text{D2})$$

$$x = \left(\frac{\rho Y_e}{B} \right)^{1/3} \quad (\text{D3})$$

where

$$f(x) = x \sqrt{x^2 + 1} (2x^2 - 3) + 3 \sinh^{-1}(x) \quad (\text{D4})$$

$$A = \frac{\pi m_e^4 c^5}{3h^3} \approx 6.0 \times 10^{22} \text{ dynes cm}^{-2}$$

$$B = \frac{8\pi m_e^3 c^3}{3h^3 N_A} \approx 9.7 \times 10^5 \text{ g cm}^{-3}.$$

Combining this equation of state with equation (D1) gives

$$\frac{1}{r^2} \frac{d}{dr} \left[r^2 \frac{d}{dr} (x^2 + 1)^{1/2} \right] = -\frac{\pi G B^2}{2AY_e^2} x^3 \quad (\text{D5})$$

where we have made the assumption that $dY_e/dr = 0$.

In order to non-dimensionalize these equations, define $z^2 = x^2 + 1$ and let z_c be the value of z at center of the

model. We also define

$$\alpha \equiv \left(\frac{2A}{\pi G} \right)^{1/2} \frac{1}{B z_c}. \quad (\text{D6})$$

and transform to the variables

$$r \equiv \alpha \zeta \quad (\text{D7})$$

$$z \equiv z_c \Phi. \quad (\text{D8})$$

This yields the differential equation

$$\frac{d}{d\zeta} \left(\zeta^2 \frac{d\Phi}{d\zeta} \right) = \frac{1}{Y_e^2} \left(\Phi^2 - \frac{1}{z_c^2} \right)^{3/2}. \quad (\text{D9})$$

At the center ($\zeta = 0$), the boundary conditions are

$$\Phi(\zeta = 0) = 1 \quad (\text{D10})$$

$$\left. \frac{d\Phi}{d\zeta} \right|_{\zeta=0} = 0 \quad (\text{D11})$$

At the surface ($\zeta = \zeta_s$), $\rho \rightarrow 0$ and so $z \rightarrow 1$, meaning

$$\Phi(\zeta = \zeta_s) = \frac{1}{z_c}. \quad (\text{D12})$$

Now, we divide the white dwarf into two zones which have different values of Y_e . By assuming a piecewise constant form for Y_e , we can continue to solve equation (D9) throughout the whole white dwarf. Specifically, we use

$$Y_e = \begin{cases} Y_{e,0} & \text{if } z < z_n \\ Y_{e,n} & \text{if } z > z_n. \end{cases} \quad (\text{D13})$$

The transition between the two zones occurs at ζ_n such that $\Phi(\zeta_n) = z_n/z_c$. The following physical conditions must be satisfied at this interface

$$P_+ = P_- \quad (\text{D14})$$

$$\left(\frac{1}{\rho} \frac{dP}{dr} \right)_+ = \left(\frac{GM_r}{r^2} \right)_-. \quad (\text{D15})$$

Note that the continuity of P implies the continuity of x , and hence z , even though Y_e is discontinuous. The dimensionless equivalents of these conditions are

$$\Phi(\zeta = \zeta_n^-) = \Phi(\zeta = \zeta_n^+) \quad (\text{D16})$$

$$\left(Y_e \frac{d\Phi}{d\zeta} \right)_{\zeta=\zeta_n^-} = \left(Y_e \frac{d\Phi}{d\zeta} \right)_{\zeta=\zeta_n^+}. \quad (\text{D17})$$

Constructing a two-zone model is now simple. Specify the three parameters for the equation of state: $Y_{e,0}$, $Y_{e,n}$, z_n . Select a central density (which sets the value of z_c) and then integrate the ODE observing the boundary and jump conditions. The solution gives the structure of a single two-zone model. A one-parameter family of models can be constructed by varying z_c , which in turn varies the properties (e.g., mass, radius) of the model.

D2 Applications of the Two-Zone Model

Our MESA models are in hydrostatic equilibrium: their evolution is occurring on timescales much longer than the dynamical time. We use the two-zone model to find approximate sequences of hydrostatic models along which the MESA models evolve. This gives us insight into the processes that control the timescale of the evolution.

The piecewise equation of state given in equation (D13) can be used to represent the $A = 24$ captures: setting $\log_{10} \rho_n = 9.6$, with $Y_{e,0} = 0.5$ and $Y_{e,n} = Y_{e,0} - X_{\text{Mg}}/12$ corresponds to instantaneous neutronization of all available ^{24}Mg at densities above the threshold density.

Fig. D1 shows the schematic evolution of models with $X_{\text{Mg}} = 0.05$. The black line is the family of two-zone hydrostatic models. This family of models is generated by varying P_c (the central pressure). Because of the discontinuity in Y_e , the continuous variation in P_c gives a discontinuous variation in ρ_c . (In Fig. D1, the density jump is hidden by point 2, but the jumps are apparent in Fig. D2.) The grey line shows the family of models without neutronization. For central densities less than ρ_n (e.g., point 1) the two families are equivalent. At point 2, the central density crosses the threshold density and the families diverge. At point 3, the model has a substantial low- Y_e core and has a much higher central density at fixed mass relative to the models without neutronization.

The numbered points in Fig. D1 represent a temporal sequence of models. The time evolution is driven by the increase in M set by accretion. For a given value of \dot{M} , the timescale for changes in ρ_c is given by equation 1, where the value of $d \ln \rho_c / d \ln M$ comes from the sequence of hydrostatic models. In Fig. 8, the black dashed line is calculated using the model without neutronization, while the black dotted line is calculated using the two zone model. This latter line does an excellent job of quantitatively describing the more rapid contraction of the MESA model following the $A = 24$ captures.

Fig. D2 shows the schematic evolution of models with $X_{\text{Mg}} = 0.15$. The black line is the family of two-zone hydrostatic models. The grey line shows the family of models without neutronization. For central densities less than ρ_n (e.g., point 1) the two families are equivalent. At point 2, neutronization begins to have an effect. At point 3, the model passes the maximum mass possible for the family of models with $\log_{10} \rho_n = 9.60$. Up to this point, as in the case with $X_{\text{Mg}} = 0.05$, the points 1-3 represent a temporal sequence of models whose time evolution is driven by increasing M .

With the equation of state held fixed, point 3 would mark the onset of dynamical instability. However, the characteristic timescale of the electron captures is longer than the dynamical time. Therefore it is not physically possible for ρ_n to remain fixed. Only material at densities where the electron capture timescale is shorter than the evolutionary timescale is able to completely neutronize.

For the large X_{Mg} models like that in Fig. D2, the evolutionary timescale becomes sufficiently short that there is no longer time for a significant amount of mass to accrete. Therefore, the evolution switches to a sequence of models with constant M , as indicated by the black dashed line and points 4-6 in Fig. D2. The fixed value of M is the maximum

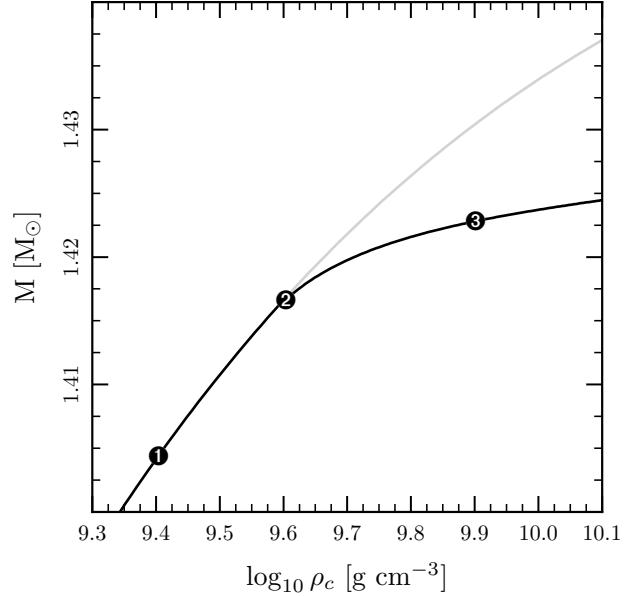


Figure D1. The black line shows the sequence of two-zone hydrostatic models with electron captures above $\log_{10} \rho_n = 9.6$ with the change in Y_e corresponding to $X_{\text{Mg}} = 0.05$. The grey line shows a zero-temperature model without neutronization. With neutronization taken into account, the central density increases more rapidly with increasing mass. The numbered points indicate a temporal series of models; specific points are discussed in more detail in the text.

mass for a model with the initial value of $\log_{10} \rho_n = 9.60$ (i.e., point 3).

The evolution along the temporal sequence of points 3-6 is limited by the electron capture rates. To describe this quantitatively, for a given ρ_c , we find the value of ρ_n that corresponds to the hydrostatic model with a given M . Then we calculate the neutronization timescale (equation 23) corresponding to this value of ρ_n . This gives the black dash dotted line shown in Fig. 8, which does a good job of reproducing the evolution observed in the MESA model. For simplicity, we used the electron capture rates at fixed temperature ($\log_{10} T = 8.6$) to calculate λ_{ec} .

The qualitatively different evolution experienced by the $X_{\text{Mg}} = 0.05$ and $X_{\text{Mg}} = 0.15$ models is due to the presence of a maximum mass in the families of two-zone models at a central density less than the critical density for ^{20}Ne captures. Calculating the central density at which this maximum occurs for each value of X_{Mg} gives the critical curve shown as a black dashed line in Fig. 9.

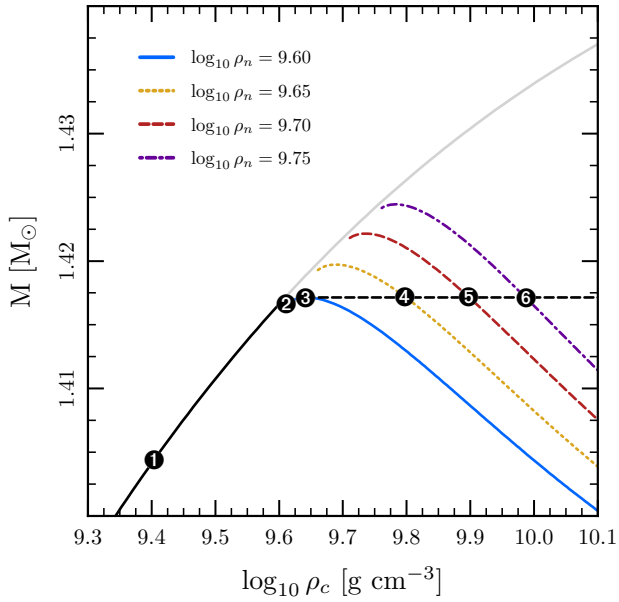


Figure D2. The black line shows the sequence of two-zone hydrostatic models corresponding to $X_{\text{Mg}} = 0.15$. The grey line shows a zero-temperature model without neutronization. The colored lines show models with neutronization at different densities. The gaps between the colored lines and the grey line are the discontinuities in ρ_c caused by the discontinuity in Y_e ; the sequence is continuous in P_c . The numbered points indicate a temporal series of models; specific points are discussed in more detail in the text. The black line changes from solid to dashed when the sequence of models changes from being defined by constant ρ_n to constant M .